

1

[ATLAS Semivisible Jets]

2

[Elena Laura Busch]

3

Submitted in partial fulfillment of the
requirements for the degree of
Doctor of Philosophy
under the Executive Committee
of the Graduate School of Arts and Sciences

4

5

6

7

8

COLUMBIA UNIVERSITY

9

2024

10

© 2024

11

[Elena Laura Busch]

12

All Rights Reserved

13

Abstract

14

[ATLAS Semivisible Jets]

15

[Elena Laura Busch]

16

Abstract of dissertation (place-holder).

Table of Contents

18	Acknowledgments	iv
19	Dedication	v
20	Introduction or Preface	1
21	Chapter 1: The Standard Model	2
22	1.1 Phenomenology: Particles and Forces	2
23	1.1.1 Particles	2
24	1.1.2 Forces	3
25	1.2 QCD and Jets	6
26	1.3 Symmetries	7
27	1.3.1 Spontaneous Symmetry Breaking and The Higgs Mechanism	8
28	1.4 Experimental Validation of the Standard Model	9
29	1.5 Limitations of the Standard Model	10
30	Chapter 2: Physics Beyond the Standard Model	12
31	2.1 Hidden Valley Models	12
32	2.2 Dark QCD	13
33	2.3 Semi-visible Jets	14

34	Chapter 3: The Large Hadron Collider	16
35	3.1 Accelerator Physics	17
36	3.1.1 The Journey of a Proton	17
37	3.1.2 Magnets	18
38	3.2 Luminosity	19
39	3.3 LHC Timeline	22
40	Chapter 4: The ATLAS Detector	24
41	4.1 Coordinate System and Geometry	24
42	4.2 Inner Detector	26
43	4.2.1 Pixel Detector	26
44	4.2.2 Semiconductor Tracker	27
45	4.2.3 Transition Radiation Tracker	27
46	4.3 Calorimeters	28
47	4.3.1 Liquid Argon Calorimeter	29
48	4.3.2 Tile Calorimeter	32
49	4.4 Muon Spectrometer	33
50	4.5 Magnet System	35
51	4.6 Forward Detectors	36
52	4.7 Trigger and Data Acquisition	37
53	Chapter 5: Particle Reconstruction and Identification	39
54	5.1 Inner Detector Tracks	39
55	5.2 Photons and Electrons	42

56	5.3 Muons	42
57	5.4 Jets	42
58	5.4.1 Calorimeter Clusters	42
59	5.4.2 Particle Flow Reconstruction	42
60	5.4.3 Jet Clustering	42
61	5.4.4 Jet Substructure	42
62	5.5 Missing Transverse Energy	42
63	Conclusion or Epilogue	43
64	References	47
65	Appendix A: Experimental Equipment	50
66	Appendix B: Data Processing	51

List of Figures

68	1.1	Diagram of the 17 particles comprising the Standard Model	3
69	1.2	Fundamental particle interactions of the three fundamental forces described by the	
70		Standard Model [2].	5
71	1.3	An example Feynmann diagram of jet production	6
72	1.4	An illustration of the “hat shaped” potential of the Higgs field, resulting in a non-	
73		zero vacuum expectation value.	8
74	2.1	Illustration of the hidden valley potential	13
75	2.2	The massive mediator particle Z' of the s-channel realization of a HV model . . .	13
76	3.1	The LHC accelerator complex at CERN [27]	18
77	3.2	The octants of the LHC and location of various beam activities [26]. Stars indicate	
78		the locations of beam collisions, and the associated detectors recording the	
79		outcome of those collisions.	19
80	3.3	(Left) Total integrated luminosity over the course of Run 2. (Right) Average num-	
81		ber of $p\bar{p}$ interactions per bunch crossing in Run 2. Each curve is weighted by the	
82		integrated luminosity for the year.	21
83	3.4	Timeline of LHC and HL-LHC activities [29]. Integrated luminosity estimates are	
84		approximate, and not reflective of the exact amount delivered to each experiment. .	23
85	4.1	ATLAS coordinate system and geometry	26
86	4.2	A 3D visualization of the structure of the ID in the barrel region [33]	27
87	4.3	ATLAS calorimetery system [34]	28

88	4.4	Diagram of a segment of the EMB, demonstrating the accordion plate arrangement [35]	30
89			
90	4.5	A LAr pulse as produced in the detector (triangle) and after shaping (curve) [35] . .	31
91			
92	4.6	Readout gap structure in HEC [35]	31
93			
94	4.7	TileCal wedge module [38]	33
95			
96	4.8	Cross section view of the muon spectrometer system [39]	34
97			
98	4.9	Layout of the barrel and endcap toroid magnets [32]	36
95	5.1	Graphic illustrating the various objects and high level features identified by ATLAS object reconstruction, and their interaction with different systems of the ATLAS detector [42]	40
96			
97	5.2	Track reconstruction seeding, finding and fitting illustration [43]	41
98			

List of Tables

100

Acknowledgements

101 Insert your acknowledgements text here. This page is optional, you may delete it if not

102 needed.

103

Dedication

104

Dedicated to my friends and family

105

Introduction or Preface

106 Insert your preface text here if applicable. This page is optional, you may delete it if not
107 needed. If you delete this page make sure to move page counter comment in thesis.tex to correct
108 location.

109

110

Chapter 1: The Standard Model

111 The Standard Model of particle physics is a universally accepted framework which explains
112 the interactions of fundamental particles. All known fundamental particles, outlined in Figure
113 1.1, are represented in the Standard Model. The model describes three of the four known forces:
114 the electromagnetic force, the weak force, and the strong force. Gravity, the fourth fundamental
115 force, is not addressed by the Standard Model. The Standard Model was primarily developed over
116 the course of the 1960s and 1970s, by combining the work of many physicists into one coherent
117 model. The Standard Model has been established as a well-tested theory by decades of experimen-
118 tal physics research.

119 This chapter will seek to introduce the phenomenology and mathematical foundations of the
120 Standard Model, and present the supporting experimental evidence. Phenomenon which are unex-
121 plained by the Standard Model such as gravity will be considered at the end of the chapter, leading
122 to an exploration of theories beyond the Standard Model in the subsequent chapter.

123 **1.1 Phenomenology: Particles and Forces**

124 1.1.1 Particles

125 A classic representation of the particles comprising the Standard Model is shown in Figure
126 1.1. The two primary particles classes are bosons (gauge bosons and the scalar Higgs boson) and
127 fermions (leptons and quarks). The bosons are carriers of fundamental forces, while the fermions
128 are the building blocks of matter. Fermions are sorted into three *generations*, and each fermion is
129 identified by a unique *flavor*.

130 Each entry in the table in Figure 1.1 is accompanied by 3 characteristic numbers: mass, charge,
131 and spin. The mass of each particle is determined to limited precision by experimental observa-

Standard Model of Elementary Particles

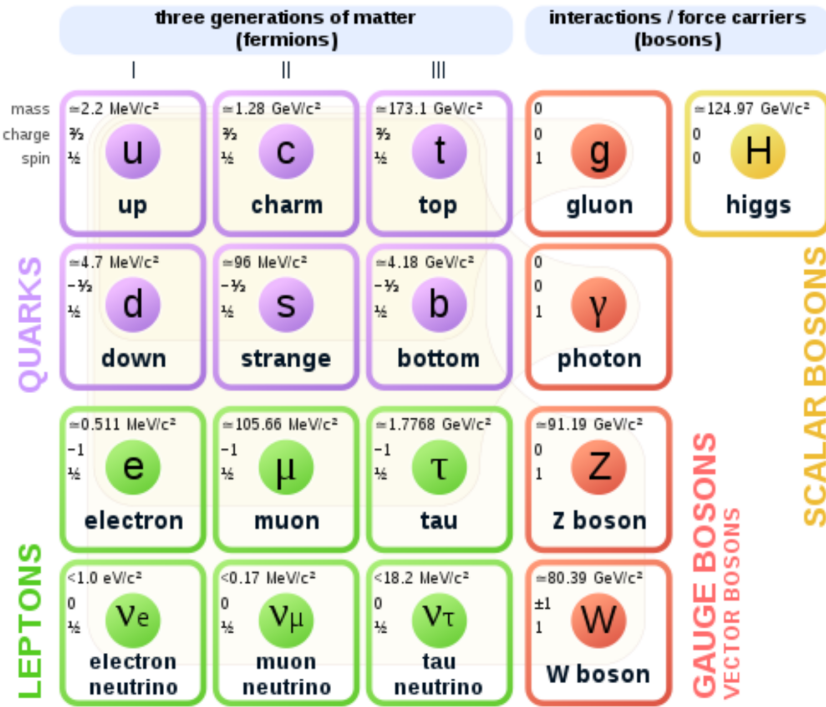


Figure 1.1: Diagram of the 17 particles comprising the Standard Model

132 tion, with the exception of photons and gluons which are known to be massless. Charge refers to
 133 the electromagnetic charge in the case of leptons and W bosons, and to color charge in the case
 134 of quarks and gluons. Spin is an intrinsic form of angular momentum carried by fundamental
 135 particles; all fermions have half integer spin, while bosons have integer spin.

136 Each particle is also known to have an *antiparticle*. Each antiparticle has the same mass but the
 137 opposite charge of their Standard Model counter part; for example, the antiparticle of the electron
 138 is the positron, which has all the same properties but a positive charge. The photon, Z boson,
 139 and Higgs are each their own antiparticle. The nature of antineutrinos is an open question driving
 140 neutrino physics research, as it is not currently known whether neutrinos are their own antiparticle.

141 1.1.2 Forces

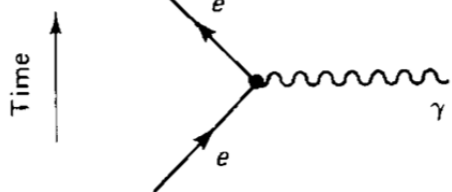
142 The three fundamental forces explained by the Standard Model are the electromagnetic force,
 143 the strong force, and the weak force. The photon is the carrier of the electromagnetic force, which

¹⁴⁴ dictates the nature of interactions between electrically charged particles, and is widely covered by
¹⁴⁵ introductory physics courses. The electromagnetic force has an infinite interaction range, a result
¹⁴⁶ of the massless and non-self interaction nature of the photon. The electromagnetic interaction is
¹⁴⁷ described by the theory of quantum electrodynamics (QED).

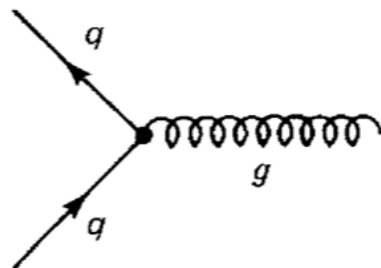
¹⁴⁸ The weak force gives rise to atomic radiation and decay. It allows for the processes of beta
¹⁴⁹ decay, which enables conversion between neutrons and protons within the nucleus of an atom. In
¹⁵⁰ the process of beta decay, a proton decays into a neutron, a positron, and a neutrino; or, a neutron
¹⁵¹ decays into a proton, an electron and an antineutrino. The weak interaction allows for quark flavor
¹⁵² mixing, the which enables beta decay. The W^+ , W^- , and Z^0 are the force carriers of the weak force.
¹⁵³ The effective range of the weak force is limited to subatomic distances, as a result of the massive
¹⁵⁴ nature of the mediator bosons. The unified theory of the electroweak interaction posits that at high
¹⁵⁵ enough energies the electromagnetic interaction and the weak force merge into the same force.
¹⁵⁶ This threshold is termed the unification energy and calculated to be about 246 GeV [1].

¹⁵⁷ The strong force confines quarks into hadron particles, such as protons and neutrons. The
¹⁵⁸ strong force also allows for the creation of atomic nuclei by binding protons and neutrons together,
¹⁵⁹ and is generally referred to as the “nuclear force” in this context. The gluon is the mediator of
¹⁶⁰ the strong force, which is a short-range force which acts at subatomic distances on the order of
¹⁶¹ 10^{-15} m. At this range, the strong force is about 100x as strong as the electromagnetic force,
¹⁶² which allows for the creation of positively charged nuclei [2]. The strong force is described by the
¹⁶³ theory of quantum chromodynamics (QCD). In the same way that QED dictates the interaction of
¹⁶⁴ electrically charges particles, QCD dictates the interactions of *color-charged* particles. Due to the
¹⁶⁵ particular importance of QCD in this thesis, this topic will be explored in detail in section 1.2.

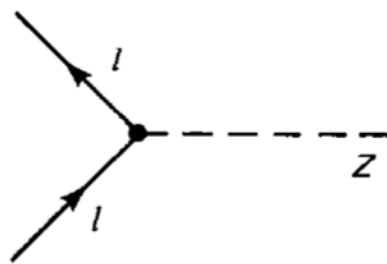
¹⁶⁶ The fundamental Feynmann diagram for each of the three forces discussed here is depicted
¹⁶⁷ in Figure 1.2. The fourth fundamental force, gravity, is not currently explained by any known
¹⁶⁸ mechanism within the Standard Model.



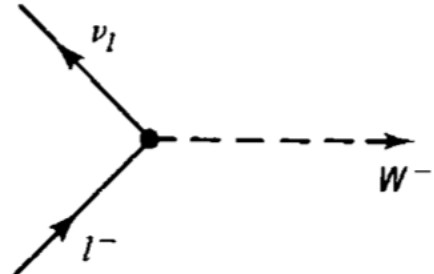
(a) The electromagnetic force



(b) The strong force



(c) The neutral weak force



(d) The charged weak force

Figure 1.2: Fundamental particle interactions of the three fundamental forces described by the Standard Model [2].

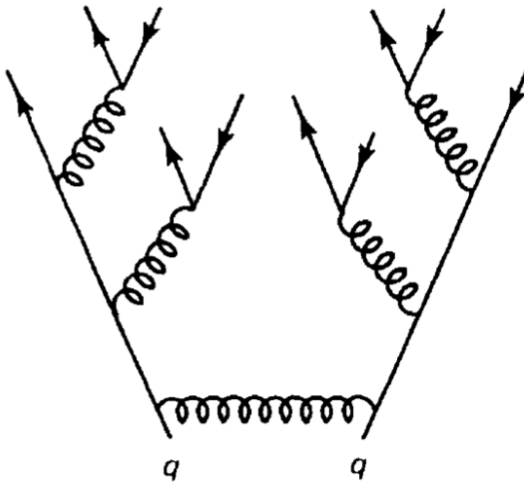


Figure 1.3: An example Feynmann diagram of jet production

¹⁶⁹ 1.2 QCD and Jets

¹⁷⁰ While there is only one type of electric charge, there are three types of color charge; red, green,
¹⁷¹ and blue. In the process $q \rightarrow q + g$, the color of the quark can change. In order to conserve color
¹⁷² charge, gluons are bicolored, and always carry some positive color charge and some negative color
¹⁷³ charge.

¹⁷⁴ Color charged particles can only exist in bound states which result in a neutral total color
¹⁷⁵ charge, a principle known as confinement. This requires that quarks and gluons exist in group
¹⁷⁶ states known as hadrons; either mesons in the case of two quarks or baryons in the case of three
¹⁷⁷ quarks. When a quark is separated from a hadron, confinement dictates that other colored objects
¹⁷⁸ are produced around the quark to obey confinement. An example of this process is shown in
¹⁷⁹ Figure 1.3. This ensemble of objects, generally a mixture of quarks and gluons, is termed a *jet*.
¹⁸⁰ Jets are among the most common phenomenon observed by detectors at hadron colliders, and their
¹⁸¹ complex structure makes them a key focus of many physics analyses.

182 **1.3 Symmetries**

183 The Standard Model is a renormalizable quantum field theory that obeys the local symmetry

184 G_{SM} :

$$G_{SM} = SU(3)_C \times SU(2)_L \times U(1)_Y. \quad (1.1)$$

185 The $SU(3)_C$ symmetry component represents the non-Abelian gauge group of QCD. There
186 are 8 generators for the $SU_C(3)$ group which correspond to 8 types of gluon, each representing a
187 different superposition of color charge [3]. The $SU(2)_L \times U(1)_Y$ symmetry group represents the
188 electroweak sector of the Standard Model, which can be spontaneously broken into the electromag-
189 netic and weak sectors. There are 4 generators for this group, which correspond to four massless
190 gauge bosons W^1 , W^2 , W^3 , and B . From these massless gauge bosons are formed the massive
191 mediators of the weak force, the W^- , W^+ and Z^0 bosons, and the massless electromagnetic force
192 carrier, the photon γ . Spontaneous symmetry breaking and the process by which gauge bosons
193 acquire mass will be addressed in section 1.3.1.

194 Noether's theorem [4] stipulates that any continuous symmetry is associated with a conserved
195 quantity. In the Standard Model, this means that the $SU(3)_C$ symmetry gives rise to conservation of
196 color charge. The $SU(2)_L \times U(1)_Y$ symmetry gives rise to conservation of electromagnetic charge.
197 Conservation of spin results from the Poincaré symmetry described by the theory of special rela-
198 tivity, which combined with Noether's theorem gives us the conversation of energy, momentum,
199 and angular momentum.

200 The SM Lagrangian is invariant under CPT symmetry, or charge, parity, and time reversal.
201 Charge conjugation (C) transform a particle into it's corresponding antiparticle by reversing the
202 charge and other quantum numbers. Parity conjugation (P) reverses spatial coordinates, which
203 transforms left-handed particles into right-handed particles and vice-versa. Time reversal (T) is
204 the theoretical process of reversing time. The L subscript in the $SU(2)_L$ group indicates that this
205 symmetry only applies to left-handed fermions. As a result, the $W^{1,2,3}$ gauge bosons of $SU(2)_L$

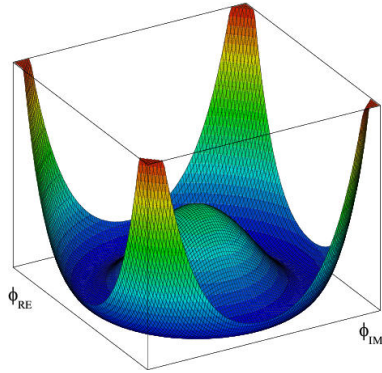


Figure 1.4: An illustration of the “hat shaped” potential of the Higgs field, resulting in a non-zero vacuum expectation value.

only interact with left handed particles, a process which maximally violates P-symmetry in the weak force. A small amount of the CP symmetry violation is also observed in the Standard Model, through the decays of strange flavored mesons [5]. The CPT theorem posits that the violation of CP symmetry implies that T-symmetry must also be violated, so that CPT is a preserved symmetry.

1.3.1 Spontaneous Symmetry Breaking and The Higgs Mechanism

Spontaneous symmetry breaking is the process by which a Lagrangian obeys a symmetry at high energies, but exhibits asymmetric behavior at lower energies. The electroweak symmetry group is spontaneously broken as $SU(2)_L \times U(1)_Y \rightarrow U(1)_{EM}$. The quantity conserved by the $SU(2)_L$ symmetry is weak isospin $T_{1,2,3}$, while the quantity conserved by $U(1)_Y$ symmetry is weak hypercharge Y . Below very high energies, the presence of the Higgs field causes the electroweak symmetry to break. The Higgs field is scalar field which forms a complex doublet of the $SU(2)$ symmetry group, with four degrees of freedom. The shape of the Higgs field potential, shown in Figure 1.4, results in a ground state with a non-zero vacuum expectation value; thus the Higgs field takes a non-zero value throughout all space, which breaks the symmetry of the weak isospin $SU(2)$ group.

The interaction with the Higgs field mixes the four massless gauge bosons $W^{1,2,3}$ and B . Three Higgs field degrees of freedom mix with the massless gauge bosons, resulting in three massive gauge bosons W^- , W^+ and Z^0 . The massless photon γ is created from the components of the

224 massless gauge bosons which do not interact with the Higgs field. The scalar Higgs boson arises
225 from the one unmixed degree of freedom the Higgs field. Spontaneous symmetry breaking also
226 violates the conservation of weak isospin and weak hypercharge, leaving only electromagnetic
227 charge ($Q = T_3 + \frac{1}{2}Y$) as a conserved quantity associated with the $U(1)_{EM}$ symmetry.

228 **1.4 Experimental Validation of the Standard Model**

229 The theoretical framework of the Standard Model coalesced into a unified theory in the mid-
230 20th century. A cascade of discoveries providing empirical evidence for the model followed
231 closely. In the 1960s, three quarks (up, down and strange) and four leptons (electron, muon,
232 and their associated neutrinos) were the known particulate building blocks of matter and the Stan-
233 dard Model. The discovery of the charm quark in 1974, through the observation of the J/ψ meson
234 [6][7], confirmed the existence of a fourth quark flavor. The discovery of the τ in 1975 [8] provided
235 the first evidence of a 3rd generation of matter. This was quickly followed by the observation of
236 the Υ meson in 1977 [9], which provided evidence for the existence of a fifth quark, the b quark
237 (bottom, or beauty). The existence of a 3rd generation of fermion also explained the observation
238 of CP violation in the weak force, as it allowed for the addition of a complex phase in the CKM
239 matrix (a unitary matrix which describes flavor mixing in the weak interaction). The top quark
240 (t) and tau neutrino (ν_τ) were predicted at this point as the final building blocks of three complete
241 generations of fermions, and they were discovered by experimental observation around the turn of
242 the 21st century [10] [11] [12].

243 The W and Z bosons were predicted by the Standard Model, but to observe them required the
244 construction of a particle accelerator powerful enough to produce them. They were finally observed
245 at CERN in 1983 by the UA1 and UA2 experiments [13] [14] at the newly constructed Super Proton
246 Synchrotron (SPS). Their masses were observed to be compatible with the masses predicted by the
247 Standard Model nearly a decade earlier. The final missing piece then was confirming the existence
248 of the Higgs, which again required the construction of a newer and more powerful collider. CERN
249 achieved this with the construction of the Large Hadron Collider (LHC), and in 2012 the ATLAS

250 and CMS experiments announced the discovery of the Higgs particle [15] [16].

251 **1.5 Limitations of the Standard Model**

252 While the Standard Model has enjoyed decades of experimental results which confirm its pre-
253 dictions, there are several glaring shortcomings. The observed phenomenon for which the Standard
254 Model provides no explanation are summarized below.

- 255 • Gravity - the Standard Model does not account for the fourth fundamental force of gravity.
- 256 • Dark Matter - there is no viable candidate to explain the existence of dark matter, a non-
257 interacting form of matter which must exist to account for gravitational observations which
258 cannot be explained by general relativity, such as the motion of galaxies, gravitational lens-
259 ing, and the structure of the universe [17].
- 260 • Matter-Antimatter asymmetry - the level of CP violation in the Standard Model isn't suf-
261 ficient to explain the large discrepancy between the amount of matter and the amount of
262 antimatter in the universe today, and the origins of this imbalance are not understood.
- 263 • Neutrino masses - the Standard Model assumes that neutrinos are massless and provides
264 no mechanism for them to acquire mass. However, observations of neutrino oscillations
265 indicates they posses some small non-zero mass [18].

266 In addition to these unexplained natural phenomenon, there are several questions about the
267 *naturalness* of the Standard Model. The principle of naturalness states that dimensionless ratios
268 between physical constants should be of order 1, and that nature should not be arbitrarily fine-
269 tuned. While this is largely an aesthetic argument, it points to many aspects of the Standard Model
270 for which there exists no natural explanation.

- 271 • Strong CP - while CP symmetry is violated in the weak force, observations indicate that it
272 is preserved by the strong force [19]. The Standard Model predicts that CP violation in the

273 strong force is possible. There is no principle which motivates this incongruity between the
274 weak force and strong force.

- 275 • Hierarchy Problem - The wide range of masses for elementary particles and the wide range of
276 scales at which the four fundamental forces operate is not motivated by the SM. Specifically,
277 it is not understood why the Higgs mass is observed to be well below the Plank scale λ ,
278 which is the energy level at which the effects of quantum gravity become significant. QFT
279 indicates that the Higgs mass is determined by contributions from all energy scales including
280 λ , meaning that its observed mass is inexplicably small.

281 The limitations of the Standard Model provide a road map for theoretical and experimental
282 particle physicists, who seek to develop new theories which account for these observations, and
283 then to find evidence which might support these *Beyond the Standard Model* (BSM) theories. The
284 next chapter will introduce the BSM theories which motivate the physics search presented in this
285 thesis.

Chapter 2: Physics Beyond the Standard Model

288 In light of the various phenomenon unexplained by the Standard Model, physicists have pro-
 289 posed various extensions to the Standard Model, collectively termed *Beyond the Standard Model*
 290 (BSM) theories. A particular focus of the physic programs at the Large Hadron Collider (LHC) are
 291 BSM models which suggest dark matter candidate particles. If these particles couple to Standard
 292 Model, they could be produced and observed at the LHC.

293 **2.1 Hidden Valley Models**

294 Hidden Valley (HV) models are a category of BSM models that allow for dark matter (DM)
 295 production at the LHC. They extend the Standard Model with an additional non-Abelian gauge
 296 group [20]. This introduces the possibility of a complex dark sector, which mirrors the complexities
 297 of Standard Model QCD, and introduces the possibility of dark quarks and gluons. The term
 298 “hidden valley” refers to the idea that the DM is hidden from the SM by a high-energy barrier, as
 299 illustrated in Figure ???. The dark sector is assumed to communicate with the Standard Model via
 300 a “portal”, or “messenger particle”, that can interact with both Standard Model and HV forces. For
 301 the s-channel scenario, the portal is considered to be a new massive mediator particle Z' .

302 The portal particle allows for the production of dark sector particles at hadron colliders. If
 303 dark quarks are produced via the decay $Z' \rightarrow q_D q_D$ they can hadronize and form dark jets. The
 304 properties of the dark jets are determined by the dynamics of the dark sector, which are explored in
 305 the subsequent section. Depending on the details of the model, the jets formed by the dark hadrons
 306 can be categorized as fully dark, semi-visible, leptonic, emerging, or other [20].

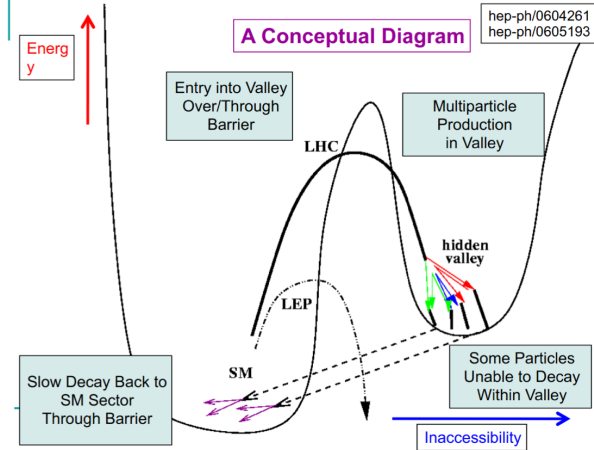


Figure 2.1: Illustration of the hidden valley potential

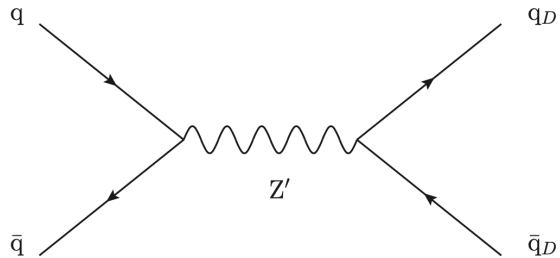


Figure 2.2: The massive mediator particle Z' of the s-channel realization of a HV model

307 2.2 Dark QCD

308 The theoretical underpinning of the semi-visible jet phenomenology is a dark sector with a
 309 gauge group $SU(N_d)$ leading to confinement at a scale Λ_d . For illustration, let's consider the
 310 case of an $SU(2)_d$ gauge theory, which gives rise to two dark fermionic generations $\chi_a = \chi_1, \chi_2$.
 311 Following the work of Timothy Cohen, et.al. we can write the fundamental dark Lagrangian as:

$$\mathcal{L}_{dark} \supset -\frac{1}{2} \text{Tr } G_{\mu\nu}^d G^{d\mu\nu} - \bar{\chi}_a (i \not{D} - M_{d,a}) \chi_a \quad (2.1)$$

312 The first term allows for the dark gluons to self-interact, while the second term enables the dark
 313 quarks to hadronize and acquire mass. The dark quarks are assumed to have a common mass M_d .
 314 The coupling strength of the strongly interacting dark quarks is termed α_d . At the confinement

315 scale Λ_d , the dark quarks can form bound states. At the scale $M_d \approx \Lambda_d$ a QCD-like show occurs.

316 The properties of the hadrons formed by the dark quarks are of particular importance to the
317 observed dark QCD dynamics. Dark-isospin number $U(1)_{1-2}$ and dark-baryon number $U(1)_{1+2}$
318 are accidental symmetries of the theory which determine the stability of the hadrons. In the case
319 of two dark flavors, six dark hadrons can be formed: four mesons ($\chi_1\bar{\chi}_1$, $\chi_2\bar{\chi}_2$, $\chi_1\bar{\chi}_2$, $\bar{\chi}_1\chi_2$) and
320 two baryons ($\bar{\chi}_1\bar{\chi}_2$, $\bar{\chi}_1\bar{\chi}_2$). The mesons $\chi_1\bar{\chi}_2$ and $\bar{\chi}_1\chi_2$ are charged under dark-isospin and will be
321 stable if this symmetry is unbroken. The baryons would also be stable as they are charged under
322 the dark-baryon number. These four stable hadrons become dark matter candidates of the theory.
323 The $\chi_1\bar{\chi}_1$ and $\chi_2\bar{\chi}_2$ mesons are not charged under either symmetry and are thus expected to decay.
324 The unstable mesons can decay into stable dark mesons, or into an off-shell Z' . The off-shell Z'
325 will then decay into two DM quarks or two SM quarks, and its products will continue to shower
326 until the final state particles are stable.

327 The number of stable and unstable dark states varies substantially depending on the details
328 of the model. The model discussed above can be generalized from $SU(2)_d$ to $SU(N)_d$, with any
329 number of colors N_c or flavors N_f . This affects the ratio of possible stable to unstable mesons,
330 which can directly impact the amount of missing energy. The fraction of missing energy is a
331 variable in many dark QCD models, and is especially important in the case of semi-visible jets.

332 2.3 Semi-visible Jets

333 A “semi-visible jet” occurs when the heavy Z' messenger particle decays into dark quarks,
334 which then hadronize in a QCD-like shower. If some of the dark hadrons are stable while others
335 decay to SM quarks via the off-shell Z' , a collimated mixture of visible and dark matter is formed
336 – this is termed a semi-visible jet. If the Z' messenger particle is produced at rest, the two jets will
337 be back-to-back in the transverse plane. If there is an imbalance in the amount of invisible particles
338 between the two jets, one of the jets will be observed to be aligned with missing transverse energy.

339 While there are a myriad of HV and dark QCD models, a handful of model parameters are most
340 important in determining the observable of these showers within a particle detector. The coupling

341 strength α_d is one of the most important, as it controls the fraction of dark hadrons emitted in the
342 shower and their average p_T . The mass of the dark quarks directly impacts the jet mass. If the
343 masses of the dark quark flavors are comparable, the ratio of stable to unstable dark hadrons will
344 be approximately 1:1. However, if there is a mass splitting, stable or unstable dark hadrons may
345 be favored, which impacts the amount of missing energy observed.

346 The ratio of stable to unstable dark hadrons in the shower is a critical variable for capturing the
347 behavior of dark showers. This value is termed r_{inv} :

$$r_{inv} = \frac{\# \text{ of stable hadrons}}{\# \text{ of hadrons}} \quad (2.2)$$

348 Events containing jets aligned with missing transverse momentum are generally considered to
349 be misreconstructed by other DM searches, and therefore discarded. This class of final states is
350 therefore largely uncovered by existing DM searches. The nature of the dark hadron shower is
351 determined by the following parameters: the Z' mass $m_{Z'}$, the Z' couplings to visible and dark
352 quarks g_q and g_{q_D} , the number of dark colors and flavors, the characteristic scale of the dark sector
353 confinement Λ_D , the scale of the dark hadrons m_D , and the average fraction of stable hadrons in
354 the decay r_{inv} . The coupling to SM quarks determines the Z' production cross section.

355

356

Chapter 3: The Large Hadron Collider

357 The Large Hadron Collider (LHC) is a 26.7 km circular high-energy particle accelerator, span-
358 ning the Swiss-French border near the city of Geneva, Switzerland [21]. The LHC occupies the
359 tunnel constructed in 1989 for the Large Electron-Positron (LEP) Collider, and reaches a maxi-
360 mum depth of 170m below the surface. The LHC is operated by the European Organization for
361 Nuclear Research (CERN), the largest international scientific collaboration in the world.

362 The LHC accelerates protons and heavy ions, and collides them at four interaction points
363 around the ring, with a design center-of-mass energy per collision of $\sqrt{s} = 14$ TeV. Each interaction
364 point is home to one of four detector experiments, which study the products of the collisions. The
365 largest of these experiments is the ATLAS detector, a general purpose detector designed to study
366 the Standard Model and search for new physics that could be produced in LHC collisions [22].
367 The CMS detector is another general purpose detector, designed and operated independently of the
368 ATLAS detector, but intended to probe the same range of physics [23]. The ALICE experiment is
369 a dedicated heavy ion experiment, and the LHC-b experiment is a dedicated *b*-physics experiment
370 [24] [25].

371 This chapter will cover the multi-component accelerator complex powering the LHC, the state-
372 of-the-art magnets which steer the particle beams, measurements of the intensity and number of
373 collisions produced by the LHC, and finally an overview of LHC activities in the past, present, and
374 future.

375 **3.1 Accelerator Physics**

376 **3.1.1 The Journey of a Proton**

377 From 2010 - 2018, the protons which fed the LHC started as hydrogen gas. The electrons were
378 removed from the hydrogen atoms through the use of strong electric fields. The linear accelerator
379 LINAC2 then accelerated the protons to an energy of 50 MeV. Between 2018 and 2020, LINAC2
380 was replaced with LINAC4, which instead accelerates H^- ions, hydrogen atoms with two electrons.
381 LINAC4 is capable of accelerating the H^- ions to 160 MeV. Before injection to the next part of
382 the acceleration chain, both electrons are stripped from the H^- ions, leaving just protons. From
383 here the protons enter the Proton Synchrotron booster, where they are accelerated up to 1.4 GeV of
384 energy. Subsequently they are sorted into bunches separated in time by 25 ns, where each bunch
385 contains approximately 10^{11} protons. Next the bunches pass through the Proton Synchrotron (PS)
386 and the Super Proton Synchrotron (SPS), where they reach energies of 25 GeV and 450 GeV
387 respectively. Finally they are injected into the LHC as two beams traveling in opposite direction.
388 The original design allowed each beam to be accelerated up to 7 TeV of energy. Due to limitations
389 in the performance of the superconducting LHC magnets, the highest energy actually achieved by
390 the LHC beams during Run 2 was 6.5 TeV, giving a collision center-of-mass energy of $\sqrt{s} = 13$
391 TeV [26]. Figure 3.1 shows the full LHC accelerator complex.

392 Acceleration in the LHC is performed by eight radio frequency (RF) cavities located around the
393 ring. Each RF cavity produces a 2 MV electric field oscillating at 40 MHz. The 40MHz oscillation
394 produces a point of stable equilibrium every 2.5 ns. These points of equilibrium are synchronized
395 with the occurrence of the proton bunches produced in the PS – a proton bunch occupies one out
396 of every ten points of stable equilibrium, such that the bunches maintain a 25 ns spacing [26].

397

The CERN accelerator complex Complexe des accélérateurs du CERN

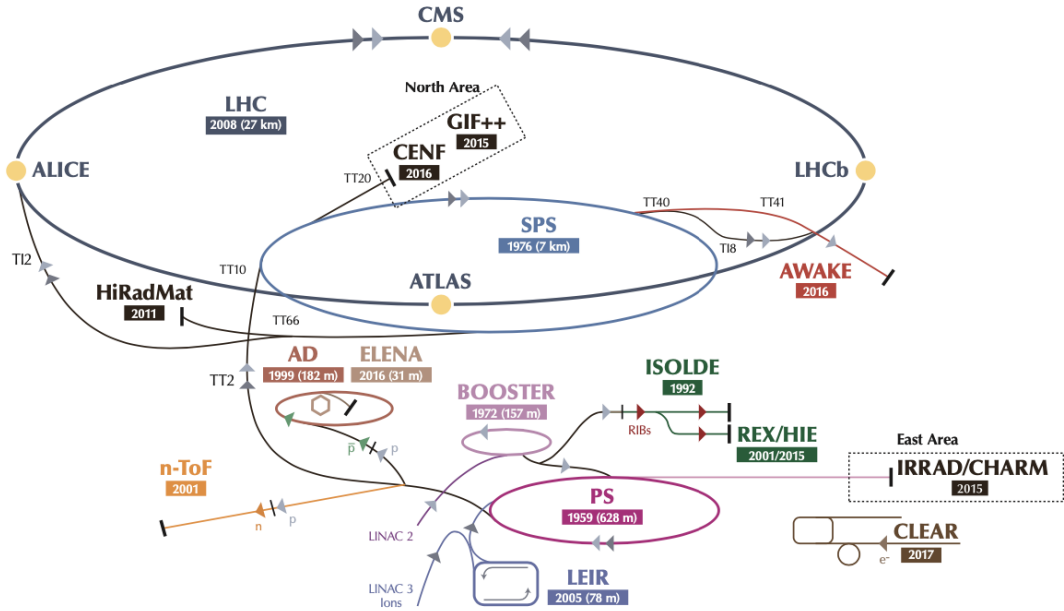


Figure 3.1: The LHC accelerator complex at CERN [27]

398 3.1.2 Magnets

399 In addition to the acceleration cavities, the LHC houses 9593 superconducting magnets which
 400 direct and focus the proton beam on its 27 kilometer journey. The magnets are comprised of super-
 401 conducting Niobium-Titanium coils cooled to 1.9K by superfluid helium. As the beams approach
 402 one of the four collision points around the ring, multipole magnets focus and squeeze the beam for
 403 optimal collisions [26].

404 The LHC is divided into sections, where each section contains an arc and a straight insertion. The arcs are composed of 1232 large dipole magnets which bend the beam
 405 to follow the roughly circular 27 km path. The main dipoles generate powerful 8.3 tesla magnetic
 406 fields to achieve this bend. Each dipole magnet is 15 meters long and weighs 35 tonnes. The
 407 dipoles work in conjunction with quadrupole magnets, which keep the particles in a focused beam,
 408 and smaller sextupole, octupole and decapole magnets which tune the magnetic field at the ends of
 409 the dipole magnets [28].

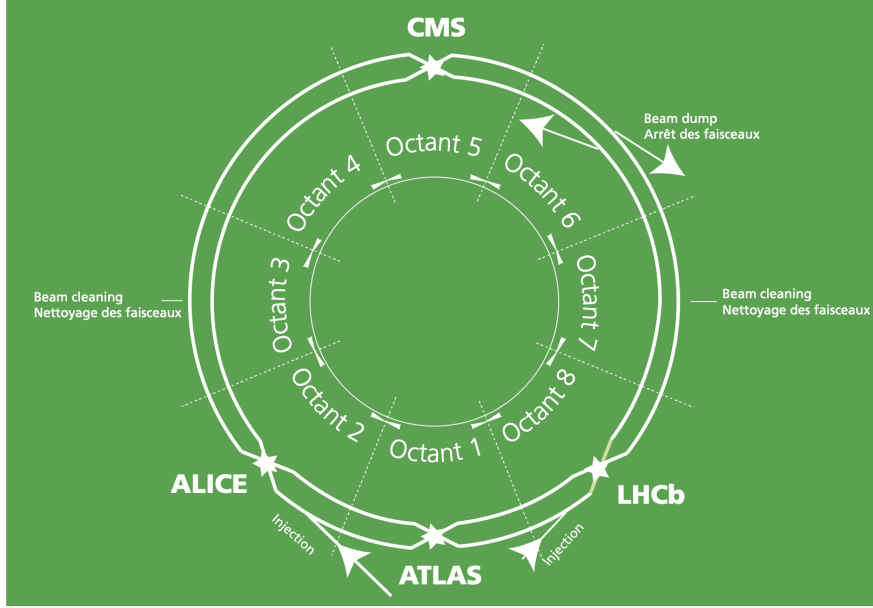


Figure 3.2: The octants of the LHC and location of various beam activities [26]. Stars indicate the locations of beam collisions, and the associated detectors recording the outcome of those collisions.

411 The straight insertion sections have different purposes depending on their location around the
 412 ring: beam collisions, beam injection, beam dumping, or beam cleaning. At the four collision
 413 points, insertion magnets squeeze the beam to ensure a highly focused collision. This is accom-
 414 plished with a triplet of quadrupole magnets, which tighten the beam from 0.2 millimeters to just
 415 16 micrometers in diameter. Insertion magnets also clean the beam, which prevents stray particles
 416 from hitting sensitive components throughout the LHC. When the LHC is ready to dispose of a
 417 beam of particles, beam dump magnets deflect the path of the beam into a straight line towards
 418 a block of concrete and graphite that stops the beam. A dilution magnet then reduces the beam
 419 intensity by a factor of 100,000 before the final stop [28]. Figure 3.2 shows the locations various
 420 beam activities.

421 3.2 Luminosity

422 Collisions at the LHC occur when the two beams of proton bunches cross at one of the four
 423 interaction points. The intensity of collisions is described by the instantaneous luminosity, the

424 formula for which is given in equation 3.1.

$$L = \frac{fN_1N_2}{4\pi\sigma_x\sigma_y} \quad (3.1)$$

425 Here f is the revolution frequency, N_1 and N_2 are the number of particle per bunch for each
426 beam, and σ_x , σ_y are the horizontal and vertical beam widths.

427 The instantaneous luminosity gives the number of the collisions that could be produced at the
428 interaction point per unit of cross-sectional area per unit of time, generally expressed in $\text{cm}^{-2}\text{s}^{-1}$.
429 The integrated luminosity is obtained by integrating the instantaneous luminosity over a given
430 block of time, and measures the total number of collisions which have occurred during that op-
431 eration period. The total integrated luminosity is directly correlated with the size of the datasets
432 collected by the LHC experiments. Total integrated luminosity for Run 2 is illustrated in Figure
433 3.3.

434 High levels of instantaneous luminosity result in multiple pp collisions per bunch crossing,
435 which leads to an effect known as *pileup*. Pileup poses a challenge for detector physics, as recon-
436 structing the products of multiple simultaneous events is far more challenging than reconstructing
437 a single event with no pileup. Pileup conditions vary from year-to-year and run-to-run of LHC op-
438 eration, and the impact of these conditions are taken into account when analyzing the data, as will
439 be discussed further in Chapter 5. Measurement of pileup conditions during Run 2 are illustrated
440 in Figure 3.3.

441 The design peak luminosity of the LHC is $1.0 \times 10^{34} \text{ cm}^{-2}\text{s}^{-1}$. During Run 1 of the LHC the
442 peak instantaneous luminosity was $0.8 \times 10^{34} \text{ cm}^{-2}\text{s}^{-1}$. Over the course of Run 1 the LHC collected
443 a total integrated luminosity of 5.46 fb^{-1} at $\sqrt{s} = 7 \text{ TeV}$, and 22.8 fb^{-1} at $\sqrt{s} = 8 \text{ TeV}$. Following the
444 first long shutdown and upgrade phase of operations, the LHC achieved a center of mass energy
445 $\sqrt{s} = 13 \text{ TeV}$ at the beginning of Run 2 in 2015. The LHC was also able to deliver 2.0×10^{34}
446 $\text{cm}^{-2}\text{s}^{-1}$ peak instantaneous luminosity, double the design value. During LHC Run 2, from 2015-
447 2018, the LHC delivered 156 fb^{-1} of integrated luminosity for proton-proton collisions. Run 3 of

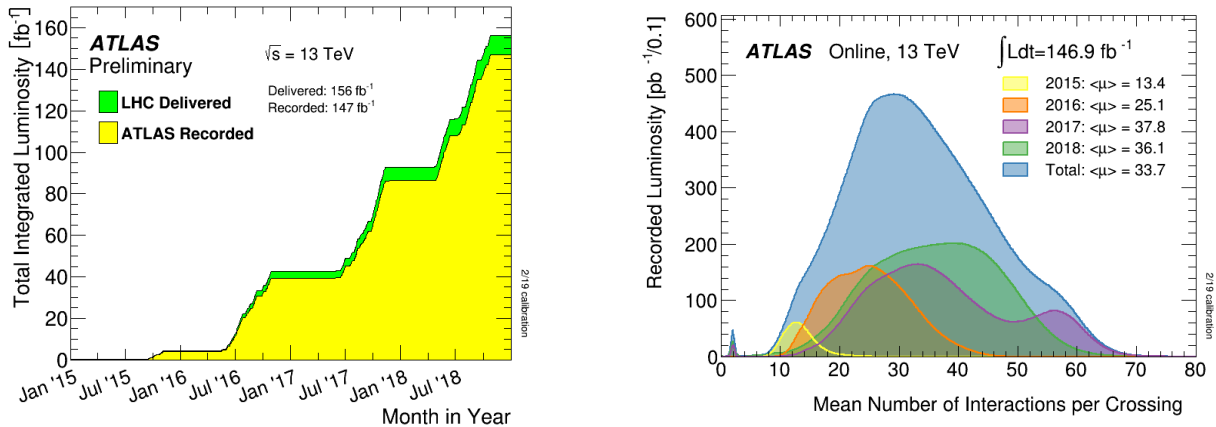


Figure 3.3: (Left) Total integrated luminosity over the course of Run 2. (Right) Average number of pp interactions per bunch crossing in Run 2. Each curve is weighted by the integrated luminosity for the year.

448 the LHC began in 2022, and is expected to deliver 250 fb^{-1} of integrated luminosity to the ATLAS
 449 and CMS experiments by 2026 [29].

450 The goal of LHC physic analyses is to find and study rare events produced by interesting
 451 physics processes. The cross section σ of a given process indicates the probability of that process
 452 occurring given the beam conditions of the LHC. Multiplying the cross section by the integrated
 453 luminosity of a dataset gives the expected number of events for that process within the dataset.

$$N_{\text{events}} = \int \sigma L(t) dt = \mathcal{L} \times \sigma \quad (3.2)$$

454 The cross section for most processes of interest, especially BSM processes, is several orders of
 455 magnitude below the total cross section for the LHC. Therefore maximizing the number of events
 456 produced in collisions is crucial to increase the likelihood of producing events from processes of
 457 interest. For this reason, maximizing instantaneous luminosity is a key factor in accelerator design
 458 and operation, while mitigating the resulting pileup effects is a key component in detector design
 459 and operation.

460 **3.3 LHC Timeline**

461 The first proton-proton collisions at the LHC were achieved in 2010 with a center-of-mass
462 energy of $\sqrt{s} = 7$ TeV. Run 1 of the LHC took place between 2010 and early 2013, during which
463 time the center-of-mass collision energy increased from 7 TeV to 8 TeV. Figure 3.4 shows an
464 overview of LHC activities beginning in 2011, in the midst of Run 1. The data collected during
465 Run 1 led to the discovery of the Higgs Boston in 2012 [30].

466 Between 2013 and 2015 the LHC underwent the first Long Shutdown (LS1) during which
467 time maintenance and renovation was performed on the accelerator chain, including the repair and
468 consolidation of the high-current splices which connect the super-conducting LHC magnets. Run
469 2 of the LHC took place from 2015 to 2018 and achieved a center-of-mass energy of $\sqrt{s} = 13$ TeV.
470 Analysis of data collected in Run 2 is still on going, and is the subject of study in this thesis.

471 Between 2018 and 2022 the LHC underwent the second Long Shutdown (LS2), allowing for
472 further detector and accelerator maintenance and upgrades. Key improvements to the LHC in-
473 cluded the improvement of the insulation for over 1200 diode magnets, and the upgrade from
474 LINAC2 to LINAC4 mentioned in Section 3.1.1. Run 3 of the LHC began in 2022 and achieved a
475 center-of-mass energy of $\sqrt{s} = 13.6$ TeV.

476 Run 3 is scheduled to continue through 2026, at which point the LHC machine and detectors
477 will undergo upgrades for the *high luminosity* LHC (HL-LHC). The HL-LHC will increase the
478 instantaneous machine luminosity by a factor of 5 - 7.5 with respect to the nominal LHC design.
479 The bottom panel of Figure 3.4 shows an overview of the preparation work for the HL-LHC that
480 has been going on concurrently with Run 1, 2, and 3 of the LHC [31].



Figure 3.4: Timeline of LHC and HL-LHC activities [29]. Integrated luminosity estimates are approximate, and not reflective of the exact amount delivered to each experiment.

481

482

Chapter 4: The ATLAS Detector

483 The ATLAS detector (**A** Toroidal **L**H**C** Apparatu**S**) is one of two general purpose physics
484 detectors designed to study the products of proton-proton collisions at the LHC. The detector is
485 composed of a variety of specialized subsystems, designed to fully capture a wide array of physics
486 processes. The apparatus is 25m high, 44m in length, and weighs over 7000 tons [32]. The LHC
487 beam pipes direct proton beams to an interaction point at the center of ATLAS, and the cylindrical
488 detector design captures a complete 360° view of the *event*, tracking all particles that result from
489 the collision.

490 The main components of the ATLAS detector are the Inner Detector (ID) which provides high
491 precision tracking of charged particles leaving the collision vertex, the calorimeter system which
492 measures the energy of electromagnetic and hadronic objects, and the Muon Spectrometer (MS)
493 which gives detailed information about muons that reach the outer radii of the detector. Two
494 magnet systems, a 2 T solenoid magnet surrounding the ID, and a 0.5-1.0 T toroid magnet system
495 situated throughout the MS, produce magnetic fields which bend the trajectory of charged particles
496 traversing the detector. In addition to the main detector components, dedicated forward detectors
497 monitor beam conditions and instantaneous luminosity, and an online trigger system reduces the
498 data rate to a manageable level for storage. Each of these components will be discussed in further
499 detail in this chapter.

500 4.1 Coordinate System and Geometry

501 The ATLAS detector employs a right hand cylindrical coordinate system. The z axis is aligned
502 with the beam line, and the x-y plane sits perpendicular to the beam line. The coordinate system
503 origin is centered on the detector, such that the origin corresponds with the interaction point of the

504 two colliding beams. The detector geometry is usually characterized by polar coordinates, where
505 the azimuthal angle ϕ spans the x-y plane. The polar angle θ represents the angle away from the
506 beam line, or z axis. $\theta = 0$ aligns with the positive z -axis, and $\phi = 0$ aligns with the positive x-axis.

507 The polar coordinate θ is generally replaced by the Lorentz invariant quantity *rapidity* or y :

$$y = \frac{1}{2} \ln\left(\frac{E + p_z}{E - p_z}\right). \quad (4.1)$$

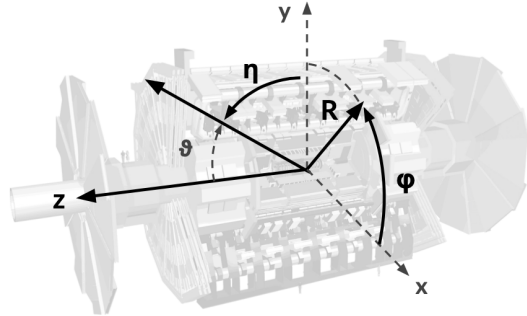
508 This substitution is advantageous because objects in the detector are traveling at highly rela-
509 tivistic speeds. The relativistic speed also means that the masses of the particles are generally small
510 compared to their total energy. In the limit of zero mass, the rapidity y reduces to the pseudorapid-
511 ity η , which can be calculated directly from the polar angle θ :

$$\eta = -\ln\left(\frac{\theta}{2}\right). \quad (4.2)$$

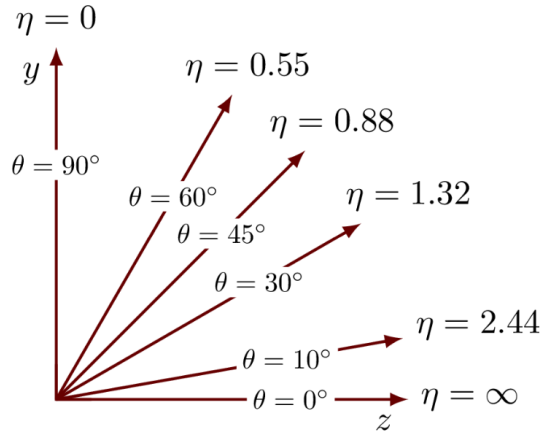
512 The distance between physics objects in the detector is generally expressed in terms of the solid
513 angle between them ΔR :

$$\Delta R = \sqrt{\Delta\phi^2 + \Delta\eta^2} \quad (4.3)$$

514 Figure 4.1a depicts the orientation of the coordinate system with respect to the ATLAS detector,
515 while Figure 4.1b illustrates the relationship between θ , η , and the beamline axis z . Direct or “head
516 on” proton-proton collisions are more likely to result in objects whose momentum is directed
517 along transverse plane (low $|\eta|$); glancing proton-proton collisions are more likely to result in
518 objects whose momentum is directed along the z -axis (high $|\eta|$). Due to the difference in the
519 nature of these collisions, as well as the cylindrical design of the ATLAS detector, the detector
520 is divided into regions of low and high η . Each subsystem has a “central” or “barrel” region
521 covering low $|\eta|$, while the “forward” or “end-cap” regions cover the area up to $|\eta| = 4.9$. Each of
522 the three main ATLAS subsystems will be discussed in the following sections.



(a) The ATLAS geometry



(b) Relationship between η and θ

Figure 4.1: ATLAS coordinate system and geometry

523 4.2 Inner Detector

524 The Inner Detector (ID) is the ATLAS subsystem closest to the interaction point. The primary
 525 purpose of the ID is to determine the charge, momentum, and trajectory of charged particles pass-
 526 ing through the detector. With this information the ID is also able to precisely determine interaction
 527 vertices.

528 The ID is composed of three sub-detectors; the Pixel Detector, the Semiconductor Tracker
 529 (SCT) and the Transition Radiation Tracker (TRT). Figure 4.2 shows the location of these three
 530 subsystems with respect to each other and the interaction point.

531 4.2.1 Pixel Detector

532 The pixel detector is the first detector encountered by particles produced in LHC collisions.
 533 The original pixel detector consists of 3 barrel layers of silicon pixels, positioned at 5 cm, 9 cm
 534 and 12 cm from the beamline. There are also 3 disks on each end-cap positioned 50 - 65 cm from
 535 the interaction point, providing full coverage for $|\eta| < 2.2$. The layers are comprised of silicon
 536 pixels each measuring $50 \times 400 \mu\text{m}^2$, with 140 million pixels in total. The pixels are organized
 537 into modules, which each contain a set of radiation hard readout electronics chips. In 2014, the
 538 Insertable B-layer (IBL) was installed, creating a new innermost layer of the pixel detector sitting

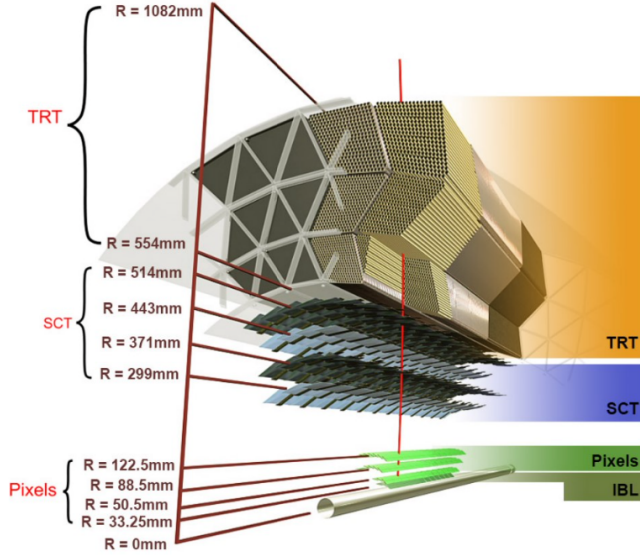


Figure 4.2: A 3D visualization of the structure of the ID in the barrel region [33]

539 just 3.3 cm from the beamline. The pixels of the IBL measure $50 \mu\text{m}$ by $250 \mu\text{m}$, and cover
 540 a pseudo-rapidity range up to $|\eta| < 3$. The IBL upgrade enhances the pixel detector's ability
 541 to reconstruct secondary vertices associated with short-lived particles such as the b-quark. The
 542 improved vertex identification also helped compensate for increasing pile-up in Run 2 [32].

543 4.2.2 Semiconductor Tracker

544 The SCT provides at least 4 additional measurements of each charged particle. It employs the
 545 same silicon technology as the Pixel Detector, but utilizes larger silicon strips which measure $80 \mu\text{m}$
 546 by 12.4 cm . The SCT is composed of 4 barrel layers, located between 30 cm and 52 cm from
 547 the beamline, and 9 end-cap layers on each side. The SCT can distinguish tracks that are separated
 548 by at least $200 \mu\text{m}$.

549 4.2.3 Transition Radiation Tracker

550 The TRT provides an additional 36 hits per particle track. The detector relies on gas filled
 551 straw tubes, a technology which is intrinsically radiation hard. The straws which are each 4 mm in
 552 diameter and up to 150 cm in length and filled with xenon gas. The detector is composed of about

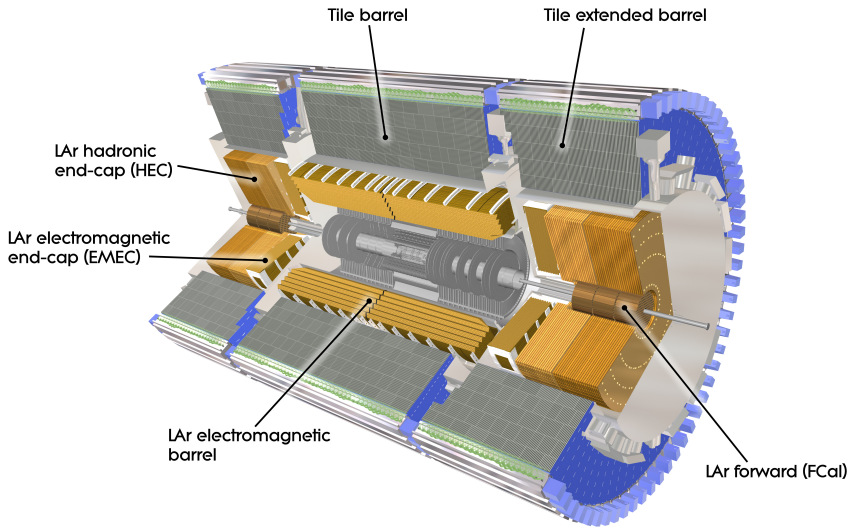


Figure 4.3: ATLAS calorimetry system [34]

553 50000 barrel region straws and 640000 end-cap straws, comprising 420000 electronic readout
 554 channels. Each channel provides a drift time measurement with a spatial resolution of $170\text{ }\mu\text{m}$ per
 555 straw. As charged particles pass through the many layers of the detector, transition radiation is
 556 emitted. The use of two different drift time thresholds allows the detector to distinguish between
 557 tracking hits and transition radiation hits.

558 4.3 Calorimeters

559 The ATLAS calorimeter system is responsible for measuring the energy of electromagnetically
 560 interacting and hadronically interacting particles passing through the detector. The calorimeters are
 561 located just outside the central solenoid magnet, which encloses the inner detectors. The calorime-
 562 ters also stop most known particles, which the exception of muons and neutrinos, preventing them
 563 from traveling to the outermost layers of the detector. The ATLAS calorimetry system is composed
 564 of two subsystems - the Liquid Argon (LAr) calorimeter for electromagnetic calorimetry and the
 565 Tile calorimeter for hadronic calorimetry. The full calorimetry system is shown in Figure 4.3.

566 4.3.1 Liquid Argon Calorimeter

567 The LAr calorimeter is a sampling calorimeter designed to trigger on and measure the ener-
568 gies of electromagnetic (EM) particles, as well as hadronic particles in the high η regions. It is
569 divided in several regions, as shown in Figure 4.3. For the region $|\eta| < 1.4$, the electromagnetic
570 barrel (EMB) is responsible for EM calorimetry, and provides high resolution energy, timing,
571 and position measurements for electrons and photons passing through the detector. The elec-
572 tromagnetic endcap (EMEC) provides additional EM calorimetry up to $|\eta| < 3.2$. In the re-
573 gion $1.4 < |\eta| < 3.2$, the hadronic endcap (HEC) provides hadronic calorimetry. For hadronic
574 calorimetry in the region $|\eta| < 1.4$, corresponding to a detector radii > 2.2 m, the less expensive
575 tile calorimeter (discussed in the next section) is used instead. A forward calorimeter (FCAL)
576 extends the hadronic calorimetry coverage up to $3.1 < |\eta| < 4.8$ [35].

577 The LAr calorimeter is composed of liquid argon sandwiched between layers of absorber mate-
578 rial and electrodes. Liquid argon is advantageous as a calorimeter active medium due to its natural
579 abundance and low cost, chemical stability, radiation tolerance, and linear response over a large
580 energy range [36]. The calorimeter is cooled to 87k by three cryostats: one barrel cryostat encom-
581 passing the EMB, and two endcap cryostats. The barrel cryostat also encloses the solenoid which
582 produces the 2T magnetic field for the inner detector. Front-end electronics are housed outside the
583 cryostats and are used to process, temporarily store, and transfer the calorimeter signals.

584 **Electromagnetic Calorimeter**

585 For the electromagnetic calorimeters, the layers of electrodes and absorber materials are ar-
586 ranged in an an accordion shape, as illustrated in Figure 4.4. The accordion shape ensures that
587 each half barrel is continuous in the azimuthal angle, which is a key feature for ensuring consistent
588 high resolution measurements. Liquid argon permeates the space between the lead absorber plates,
589 and a multilayer copper-polymide readout board runs through the center of the liquid argon filled
590 gap.

591 The detection principle for the LAr calorimeter is the current created by electrons which are

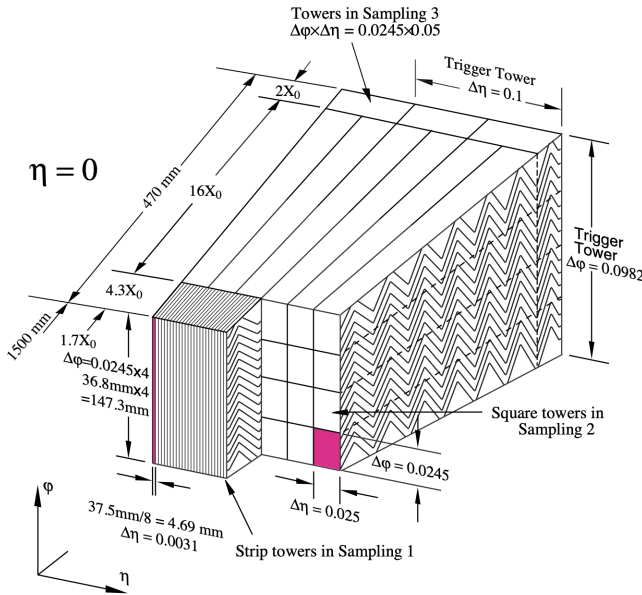


Figure 4.4: Diagram of a segment of the EMB, demonstrating the accordion plate arrangement [35]

592 released when a charged particle ionizes the liquid argon. In the barrel region, the electrons are
 593 driven towards the center electrodes by a 2000 V potential with a drift time of less than 450 ns [37].
 594 In the end-caps the voltage varies as a function of the radius in order to maintain a flat response
 595 [35]. The amount of current produced by the ionized electrons is proportional to the energy of
 596 the particle creating the signal. Figure 4.5 shows the shape of the signal produced in the LAr
 597 calorimeter, before and after it undergoes shaping during the readout process. The shaping of the
 598 pulse enforces a positive peak and a negative tail, which ensures that subsequence pulses can be
 599 separated with the precision required for the 25 ns LHC bunch spacing [35].

600 Hadronic End-cap Calorimeter

601 The HEC sits radially beyond the EMEC. The copper absorber plates in the HEC are oriented
 602 perpendicular to the beamline, with LAr as the active medium. Each end-cap is divided into two
 603 independent wheels; the inner wheel uses 25 mm copper plates, while the outer wheel uses 50 mm
 604 plates as a cost saving measure. In each wheel, the 8.5 mm plate gap is crossed by three parallel

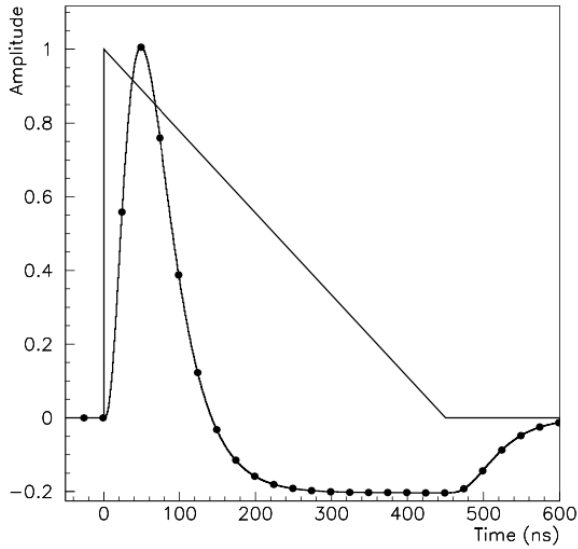


Figure 4.5: A LAr pulse as produced in the detector (triangle) and after shaping (curve) [35]

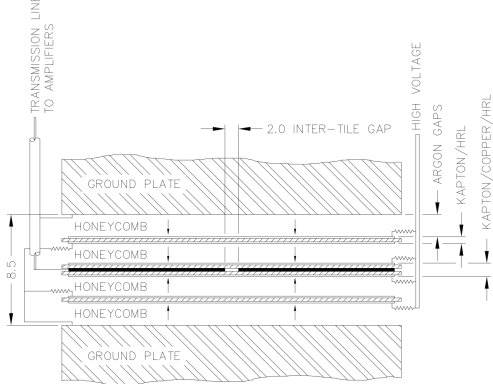


Figure 4.6: Readout gap structure in HEC [35]

605 electrodes, creating an effective drift distance of 1.8 mm. This gap is illustrated in Figure 4.6.
 606 Each wheel is divided into 32 wedge-shaped modules, each containing their own set of readout
 607 electronics.

608 **Forward Calorimeter**

609 The forward range is covered by the FCal, which provides both EM and hadronic calorimetry.
 610 It is composed of three active cylindrical modules; one EM module with copper absorber plates,
 611 and two hadronic modules with tungsten absorber plates. The plates are oriented perpendicular to

612 the beamline, and LAr is used as the active material throughout. The electrodes of the FCal consist
613 of tubes that run parallel to the beam line, arranged in a honeycomb pattern. The resulting LAr
614 gaps are as small as $250 \mu\text{m}$, which enables the FCal to handle the large influx of particles in the
615 forward region [35].

616 4.3.2 Tile Calorimeter

617 The Tile Calorimeter (TileCal) provides hadronic calorimetry in the region $\eta < 1.7$, and sur-
618 rounds the LAr calorimeter. It is responsible for measurements of jet energy and jet substructure,
619 and also plays an important role in electron isolation and triggering (including muons) [38]. Tile-
620 Cal is composed of 3 sections, as shown in Figure 4.3; a barrel calorimeter sits directly outside the
621 LAr EMB and provides coverage up to $\eta < 1.0$. Two extended barrel sections sit outside the LAr
622 endcaps and cover the region $0.8 < \eta < 1.7$.

623 TileCal is a sampling calorimeter composed of steel and plastic scintillator plates as illustrated
624 in Figure 4.7. A total of 460,000 scintillators are read out by wavelength-shifting fibers. The
625 fibers are gathered to define cells and in turn read out by photomultiplier tubes, which amplify
626 the signal and convert it to an electrical signature. Each cell has an approximate granularity of
627 $\Delta\eta \times \Delta\phi = 0.1 \times 0.1$. Each barrel is divided azimuthally into 64 independent modules, an example
628 of which is show in Figure 4.7. The modules are each serviced by front-end electronic housed in a
629 water-cooled drawer on the exterior of the module.

630 The detection principle of the TileCal is the production of light from hadronic particles inter-
631 acting with the scintillating tiles. When a hadronic particle hits the steel plate, a shower of particles
632 are produced. The interaction of the shower with the plastic scintillator produces photons, the num-
633 ber and intensity of which are proportional to the original particle's energy.

634

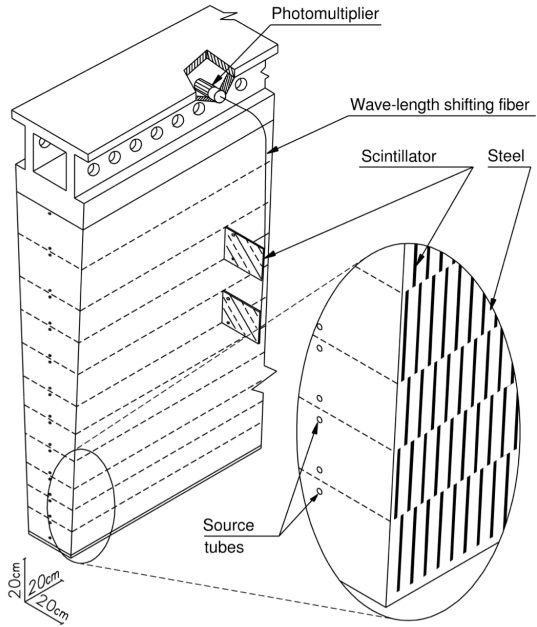


Figure 4.7: TileCal wedge module [38]

635 4.4 Muon Spectrometer

636 Unlike electrons, photons, and hadrons, muons interact minimally with the ATLAS calorimeters,
 637 and can pass through large amounts of detector material without stopping. The ATLAS Muon
 638 Spectrometer (MS) provides additional tracking information to improve the identification and mea-
 639 surement of muons. The MS comprises the outermost layers of the detector, and is interspersed
 640 with toroid magnets (discussed in Section 4.5), which provide a magnetic field of approximately
 641 0.5 T. The magnetic field bends the trajectory of the muons as they pass through the detector, and
 642 the degree of the bend is directly correlated with the muon momentum. The path of the muon is
 643 primarily measured by hits in three layers of Monitored Drift Tube (MDT) precision chambers,
 644 which cover the range $|\eta| < 2.7$. The barrel layout of the MS is show in Figure 4.8.

645 Muon triggering is provided by three layers of Resistive Plate Chambers (RPC) in the barrel
 646 ($|\eta| < 1.05$), and 3 - 4 layers of Thin Gap Chambers (TGC) in the end-caps ($1.05 < |\eta| < 2.4$).
 647 RPCs and TGCs also provide muon track measurements in the non-bending coordinate (ϕ). RPCs
 648 are constructed from two parallel resistive plates separated by a 2mm gap filled with a sensitive

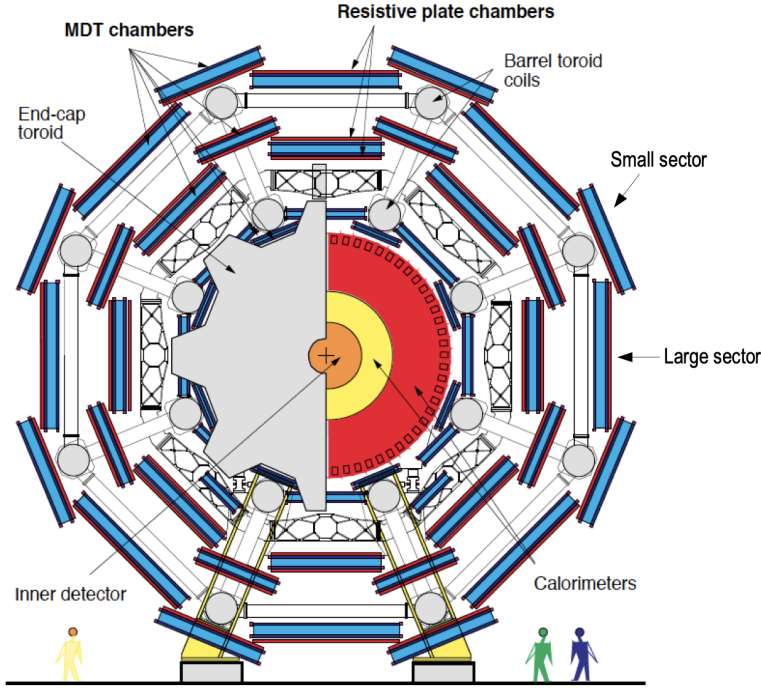


Figure 4.8: Cross section view of the muon spectrometer system [39]

649 gas mixture. This provides a total of six independent measurements for each muon track, with a
 650 spatial resolution of ~ 1 cm and a time resolution of ~ 1 ns. Time measurements from the RPCs
 651 are primarily associated to hits in the MDT precision chambers to determine the bunch crossing.
 652 The time measurement is also used to reject cosmic muons, and to search for delayed signals.
 653 TCGs provide triggering in the end-cap regions, and consist of parallel $30\ \mu\text{m}$ wires suspended
 654 in a sensitive gas mixture. TCGs provide high radiation tolerance and a fast response time, both
 655 features that are necessary for handling the high flux of muons in the forward region [39].

656 Precision measurements of muon momentum and position are primarily achieved by MDTs.
 657 The MDTs are constructed from 30 mm diameter tubes, permeated by a gas mixture of 93% Ar and
 658 7% CO₂. The average single-tube spatial resolution is $80\ \mu\text{m}$. Each chamber consists of six drift
 659 tube layers, which together provide a muon track segment resolution of $35\ \mu\text{m}$. The momentum
 660 of the muons can be calculated from the bend in the muon trajectory as they pass through the
 661 0.5T magnetic field provided by the toroids. For a $p_T = 1$ TeV track, the average p_T resolution is
 662 11%. In the inner most end-cap wheels, Cathode Strip Chambers (CSC) are used instead of MDTs,

663 covering the region $2.0 < |\eta| < 2.7$. CSCs are multi-wire proportional chambers, with a cathode
664 strip readout. The CSCs have a spatial resolution in the range of $50 \mu\text{m}$, and a maximum drift time
665 of about 30 ns, which makes them superior for handling the high flux of particles in the forward
666 region [40].

667 **4.5 Magnet System**

668 The ATLAS magnet system consists of four sets of superconducting magnets: a barrel solenoid,
669 a barrel toroid, and two end-cap toroids. The solenoid magnet produces a 2T magnetic field re-
670 sponsible for bending the trajectories of charged particles as they pass through the inner detector.
671 The three toroid magnets provide a field of 0.5 - 1 T and curve the path of muons passing through
672 the muon spectrometer.

673 The inner solenoid magnet is composed of over 9 km of niobium-titanium superconductor
674 wires, which are imbedded into strengthen pure aluminum strips. The solenoid is just 4.5 cm
675 thick, which minimizes interactions between the magnet material and particles passing through the
676 detector. It is housed in the LAr cryostat, as described in section 4.3.1, which further reduces the
677 amount of non-detector material required to support the solenoid. The return yoke of the magnet
678 is provided by the iron absorber of the TileCal [41].

679 The central ATLAS toroid magnet, providing the magnetic field for the barrel region of the MS,
680 is the largest toroidal magnet ever constructed at 25 m in length. The toroid is composed of eight
681 individual coils, each housed in their own cryostat. The toroidal magnetic field is advantageous
682 as the direction of the field is almost perpendicular to the path of the charged particles. 56 km of
683 aluminum stabilized niobium-titanium-copper superconductor wire compose the magnet. In each
684 end-cap, eight smaller superconducting coils extend the toroidal magnetic field to particles leaving
685 the detector in the forward direction [41]. Figure 4.9 shows the layout of the toroid magnets.

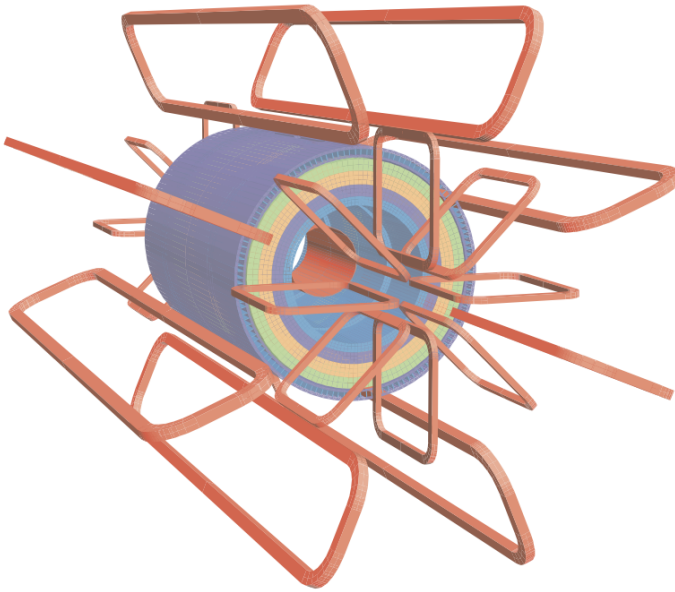


Figure 4.9: Layout of the barrel and endcap toroid magnets [32]

686 4.6 Forward Detectors

687 In addition to the inner detector, calorimeters, and muon spectrometer, three smaller detectors
688 provide coverage in the very forward region. The innermost forward detector, at 17 m from the
689 interaction point, is the **L**Uminosity measurement using **C**erenkov **I**ntegrating **D**etector (LUCID).
690 LUCID's primary purpose is to measure the relative online-luminosity for the ATLAS detector,
691 from inelastic $p - p$ scattering. The detector is composed of 20 aluminum Cerenkov tubes which
692 surround the beam pipe and face towards the interaction point.

693 The second forward detector is the Zero-Degree Calorimeter (ZDC), located 140 m from the
694 interaction point in both directions, at the point where the LHC beam-pipe divides into two separate
695 pipes. The ZDC's primary purpose is to detect forward neutrons from heavy ion collisions.

696 The third forward detector is the Absolute Luminosity For ATLAS (ALFA) system, located 240
697 m from the interaction point in both directions. ALFA determines luminosity by measuring elastic
698 scattering at small angles, from which luminosity can be calculated via the optical theorem. The
699 detector is built from scintillating fiber trackers. These are connected to the accelerator vacuum

700 via Roman pots, which allow the detector to come as close as 1mm to the beam without disrupting
701 the machine vacuum. The LUCID and ALFA detectors are crucial to determining the real-time
702 conditions of the beams and the total luminosity delivered to the ATLAS detector [32].

703 **4.7 Trigger and Data Acquisition**

704 The trigger and Data Acquisition systems (TDAQ) are responsible for selecting the most viable
705 events to save for further downstream processing. Because of the high luminosities delivered to
706 the ATLAS detector, not all events recorded can be saved; the 40 MHz bunch crossing rate must
707 be reduced by 5 orders of magnitude to an event storage rate of \sim 1 kHz. The trigger system is
708 composed of three distinct levels: Level 1 (L1), Level 2 (L2) and the event filter. Collectively the
709 L2 trigger and the event filter form the High Level Trigger (HLT).

710 The L1 trigger is implemented in the hardware of the ATLAS calorimeter and muon systems.
711 The primary modality of the L1 trigger is to identify muons, electrons, photons, jets, and τ -leptons
712 with high transverse momentum. Particles with high transverse momentum are more likely to
713 originate from direct, high energy collisions, which are most likely to produce interesting physics
714 processes. The L1 trigger also identifies events with large missing transverse energy, which could
715 be indicative of new physics. The L1 muon trigger (L1Muon) relies on RPC and TGC trigger
716 chambers in the barrel and end-cap regions of the muon spectrometer. The L1 Calorimeter Trigger
717 (L1Calo) uses reduced granularity information collected by all the calorimeter subsystems. Results
718 from the L1Muon and L1Calo triggers are combined by the Central Trigger Processor (CTP),
719 which implements a trigger ‘menu’, listing various combinations of trigger requirements. The
720 maximum L1 acceptance rate is 75 kHz, and the L1 trigger decision must reach the front-end
721 electronics within $2.5 \mu\text{s}$ of its associated bunch-crossing [32].

722 The L1 trigger defines a Region-of-Interest (RoI) for each passing event. The ROI is repre-
723 sented by the η - ϕ detector region where interesting features were identified by the L1 selection
724 process. Information about the type of feature identified and the threshold which was exceeded to
725 trigger the L1 response is also recorded. The ROI data is sent to the L2 trigger, which uses all of

726 the available information within the ROI at full granularity and precision. The L2 trigger reduces
727 the event rate from 75 kHz to 3.5 kHz, with an average processing time of 40 ms. The final stage of
728 the HLT is the event filter, which reduces the event rate to 200 Hz. The event filter uses an offline
729 analysis process to select fully rebuilt events which will be saved for further analysis.

730 All levels of the ATLAS trigger system depend on specialized electronics. Each detector front-
731 end system has a specialized Readout Driver (ROD) which collects information from several front-
732 end data streams at once. The ROD is composed of front-end analogue processing, an L1 buffer
733 which retains the information long enough for the L1 trigger decision, and dedicated links which
734 send the front-end L1 triggered data to Data Acquisition System (DAQ). Any digital signals are
735 formatted as raw data before being transferred to the DAQ. The first stage of the DAQ temporarily
736 stores the L1 data in local buffers. The ROI data is then requested by the L2 trigger, after which
737 selected events are transferred to an event building system, before events passing the event filter
738 are sent to the CERN computer center for permanent storage. The DAQ system not only allows
739 for the readout of detector data, but is also responsible for the monitoring and configuration of
740 the hardware and software components which make up the data readout system via the Detector
741 Control System (DCS).

742 The DCS allows centralized control of all detector subsystems simultaneously. It continually
743 monitors operational conditions, reports any abnormal behavior to the operator, and can perform
744 both automatic and manual interventions. The DCS reports on real time detector conditions such
745 as high or low voltage detector electronics, gas and cooling systems, magnetic field conditions,
746 humidity and temperature. This information is continually monitored by experts in the ATLAS
747 control room, so that action can be taken immediately to correct any issues that arise. The DCS also
748 handles communication between detector systems, and other systems such as the LHC accelerator,
749 the ATLAS magnets, and CERN technical services [32].

Chapter 5: Particle Reconstruction and Identification

752 With a design luminosity of $1.0 \times 10^{34} \text{ cm}^{-2}\text{s}^{-1}$, and a peak Run-2 instantaneous luminosity of
 753 $2.0 \times 10^{34} \text{ cm}^{-2}\text{s}^{-1}$, reconstructing and identifying the products of LHC pp collisions is one of the
 754 most complex tasks for each LHC experiment. The accurate reconstruction and identification of
 755 physics objects lays the ground work for all subsequent physics analyses, so it is also one of the
 756 most fundamentally important tasks performed by an experiment.

757 Reconstruction is the process of combining raw and uncalibrated hits across various subsys-
 758 tems into specific unique objects. Two particular subsystems, the Inner Detector (ID) tracker and
 759 the calorimeter play particularly important roles and will be discussed in detail. Analysis of the
 760 properties of the reconstructed objects identifies them as photon, electrons, muons, or jets. While
 761 photons, electrons, and muons are fundamental particles, jets represent a collimated shower of
 762 many hadronic particles, whose definition is more flexible. Jet reconstruction, clustering and sub-
 763 structure are all of particular important to jet identification, and to the later content of this thesis.
 764 Finally, reconstruction also identifies missing transverse energy E_T^{miss} in events, which is a crucial
 765 variable for BSM physics searches. Figure 5.1 shows how the various physics objects listed here
 766 interact with various systems in the ATLAS detector.

767 5.1 Inner Detector Tracks

768 As the inner most layer of the detector, the ID measures charged particles close to the interac-
 769 tion point. The various hits of these charged particles throughout the ID are used to reconstruct
 770 *tracks* which give the trajectories of charged particles. Track reconstruction begins by clustering
 771 hits in the Pixel and SCT detectors, and combining clusters from different radial layers of these de-
 772 tector. The multi-layer clusters form track *seeds*, which provide initial estimates of measurements

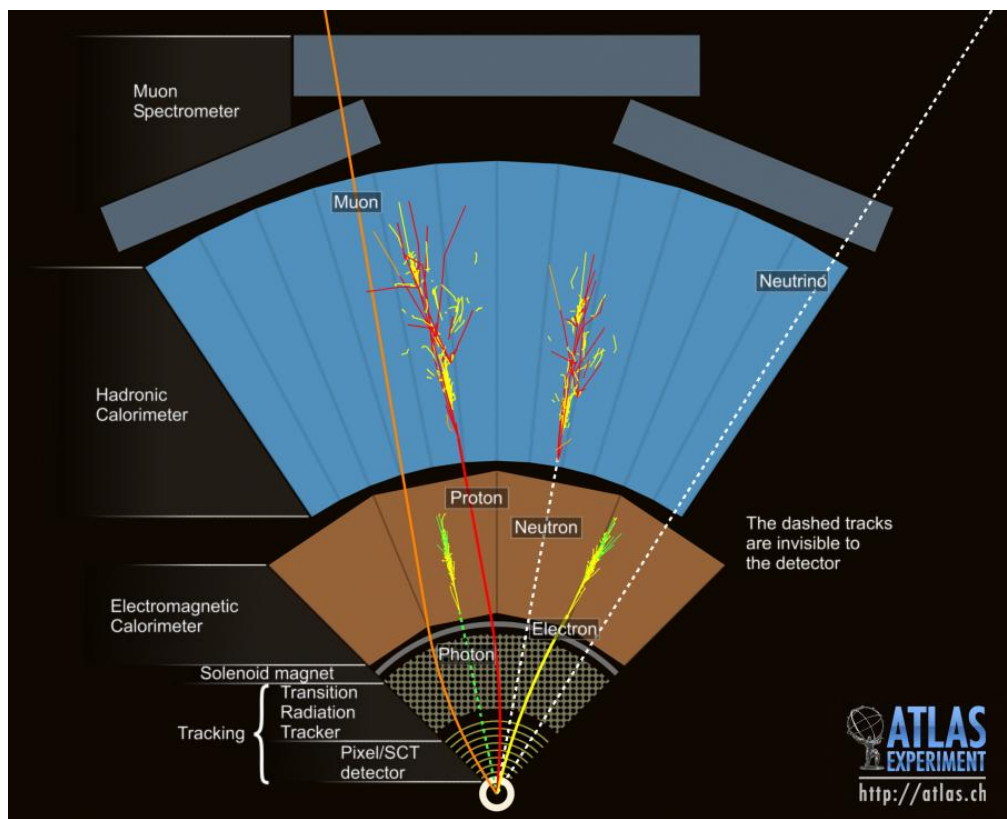


Figure 5.1: Graphic illustrating the various objects and high level features identified by ATLAS object reconstruction, and their interaction with different systems of the ATLAS detector [42]

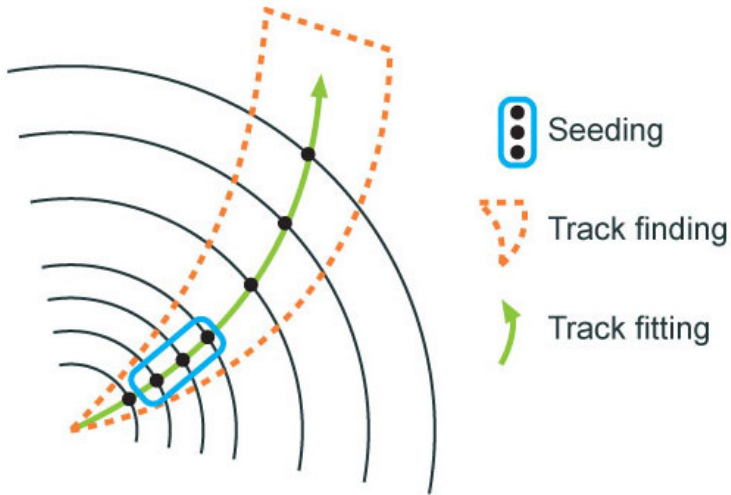


Figure 5.2: Track reconstruction seeding, finding and fitting illustration [43]

773 belonging to an individual track. The requirement of three points allows for a rough estimate of
 774 the track p_T to be made by calculating the curvature of the track and accounting of the magnetic
 775 field in the ID.

776 Tracks seeds are subject to a variety of quality requirements, such as having a minimum esti-
 777 mated p_T and passing interaction region compatibility criterion. If these requirements are satisfied,
 778 the track seeds are passed to the track finding and fitting algorithms. The interplay of these three
 779 track reconstruction steps is illustrated in Figure 5.2.

780 **5.2 Photons and Electrons**

781 **5.3 Muons**

782 **5.4 Jets**

783 **5.4.1 Calorimeter Clusters**

784 **5.4.2 Particle Flow Reconstruction**

785 **5.4.3 Jet Clustering**

786 **5.4.4 Jet Substructure**

787 **5.5 Missing Transverse Energy**

Conclusion or Epilogue

789 Use this page for your epilogue or conclusion if applicable; please use only one of the titles
790 for this page. Otherwise, you may delete it. Use this page for your epilogue or conclusion if
791 applicable; please use only one of the titles for this page. Otherwise, you may delete it. Use this
792 page for your epilogue or conclusion if applicable; please use only one of the titles for this page.
793 Otherwise, you may delete it. Use this page for your epilogue or conclusion if applicable; please
794 use only one of the titles for this page. Otherwise, you may delete it. Use this page for your
795 epilogue or conclusion if applicable; please use only one of the titles for this page. Otherwise,
796 you may delete it. Use this page for your epilogue or conclusion if applicable; please use only one
797 of the titles for this page. Otherwise, you may delete it. Use this page for your epilogue or
798 conclusion if applicable; please use only one of the titles for this page. Otherwise, you may delete
799 it. Use this page for your epilogue or conclusion if applicable; please use only one of the titles for
800 this page. Otherwise, you may delete it. Use this page for your epilogue or conclusion if
801 applicable; please use only one of the titles for this page. Otherwise, you may delete it. Use this
802 page for your epilogue or conclusion if applicable; please use only one of the titles for this page.
803 Otherwise, you may delete it. Use this page for your epilogue or conclusion if applicable; please
804 use only one of the titles for this page. Otherwise, you may delete it. Use this page for your
805 epilogue or conclusion if applicable; please use only one of the titles for this page. Otherwise,
806 you may delete it. Use this page for your epilogue or conclusion if applicable; please use only one
807 of the titles for this page. Otherwise, you may delete it. Use this page for your epilogue or
808 conclusion if applicable; please use only one of the titles for this page. Otherwise, you may delete

809 it. Use this page for your epilogue or conclusion if applicable; please use only one of the titles for
810 this page. Otherwise, you may delete it. Use this page for your epilogue or conclusion if
811 applicable; please use only one of the titles for this page. Otherwise, you may delete it. Use this
812 page for your epilogue or conclusion if applicable; please use only one of the titles for this page.
813 Otherwise, you may delete it. Use this page for your epilogue or conclusion if applicable; please
814 use only one of the titles for this page. Otherwise, you may delete it. Use this page for your
815 epilogue or conclusion if applicable; please use only one of the titles for this page. Otherwise,
816 you may delete it. Use this page for your epilogue or conclusion if applicable; please use only one
817 of the titles for this page. Otherwise, you may delete it. Use this page for your epilogue or
818 conclusion if applicable; please use only one of the titles for this page. Otherwise, you may delete
819 it. Use this page for your epilogue or conclusion if applicable; please use only one of the titles for
820 this page. Otherwise, you may delete it. Use this page for your epilogue or conclusion if
821 applicable; please use only one of the titles for this page. Otherwise, you may delete it. Use this
822 page for your epilogue or conclusion if applicable; please use only one of the titles for this page.
823 Otherwise, you may delete it. Use this page for your epilogue or conclusion if applicable; please
824 use only one of the titles for this page. Otherwise, you may delete it. Use this page for your
825 epilogue or conclusion if applicable; please use only one of the titles for this page. Otherwise,
826 you may delete it. Use this page for your epilogue or conclusion if applicable; please use only one
827 of the titles for this page. Otherwise, you may delete it. Use this page for your epilogue or
828 conclusion if applicable; please use only one of the titles for this page. Otherwise, you may delete
829 it. Use this page for your epilogue or conclusion if applicable; please use only one of the titles for
830 this page. Otherwise, you may delete it. Use this page for your epilogue or conclusion if
831 applicable; please use only one of the titles for this page. Otherwise, you may delete it. Use this
832 page for your epilogue or conclusion if applicable; please use only one of the titles for this page.
833 Otherwise, you may delete it. Use this page for your epilogue or conclusion if applicable; please
834 use only one of the titles for this page. Otherwise, you may delete it. Use this page for your
835 epilogue or conclusion if applicable; please use only one of the titles for this page. Otherwise,

836 you may delete it. Use this page for your epilogue or conclusion if applicable; please use only one
837 of the titles for this page. Otherwise, you may delete it. Use this page for your epilogue or
838 conclusion if applicable; please use only one of the titles for this page. Otherwise, you may delete
839 it. Use this page for your epilogue or conclusion if applicable; please use only one of the titles for
840 this page. Otherwise, you may delete it. Use this page for your epilogue or conclusion if
841 applicable; please use only one of the titles for this page. Otherwise, you may delete it. Use this
842 page for your epilogue or conclusion if applicable; please use only one of the titles for this page.
843 Otherwise, you may delete it. Use this page for your epilogue or conclusion if applicable; please
844 use only one of the titles for this page. Otherwise, you may delete it. Use this page for your
845 epilogue or conclusion if applicable; please use only one of the titles for this page. Otherwise,
846 you may delete it. Use this page for your epilogue or conclusion if applicable; please use only one
847 of the titles for this page. Otherwise, you may delete it. Use this page for your epilogue or
848 conclusion if applicable; please use only one of the titles for this page. Otherwise, you may delete
849 it. Use this page for your epilogue or conclusion if applicable; please use only one of the titles for
850 this page. Otherwise, you may delete it. Use this page for your epilogue or conclusion if
851 applicable; please use only one of the titles for this page. Otherwise, you may delete it. Use this
852 page for your epilogue or conclusion if applicable; please use only one of the titles for this page.
853 Otherwise, you may delete it. Use this page for your epilogue or conclusion if applicable; please
854 use only one of the titles for this page. Otherwise, you may delete it. Use this page for your
855 epilogue or conclusion if applicable; please use only one of the titles for this page. Otherwise,
856 you may delete it. Use this page for your epilogue or conclusion if applicable; please use only one
857 of the titles for this page. Otherwise, you may delete it. Use this page for your epilogue or
858 conclusion if applicable; please use only one of the titles for this page. Otherwise, you may delete
859 it. Use this page for your epilogue or conclusion if applicable; please use only one of the titles for
860 this page. Otherwise, you may delete it. Use this page for your epilogue or conclusion if
861 applicable; please use only one of the titles for this page. Otherwise, you may delete it. Use this
862 page for your epilogue or conclusion if applicable; please use only one of the titles for this page.

863 Otherwise, you may delete it. Use this page for your epilogue or conclusion if applicable; please
864 use only one of the titles for this page. Otherwise, you may delete it. Use this page for your
865 epilogue or conclusion if applicable; please use only one of the titles for this page. Otherwise,
866 you may delete it. Use this page for your epilogue or conclusion if applicable; please use only one
867 of the titles for this page. Otherwise, you may delete it. Use this page for your epilogue or
868 conclusion if applicable; please use only one of the titles for this page. Otherwise, you may delete
869 it. Use this page for your epilogue or conclusion if applicable; please use only one of the titles for
870 this page. Otherwise, you may delete it. Use this page for your epilogue or conclusion if
871 applicable; please use only one of the titles for this page. Otherwise, you may delete it. Use this
872 page for your epilogue or conclusion if applicable; please use only one of the titles for this page.
873 Otherwise, you may delete it. Use this page for your epilogue or conclusion if applicable; please
874 use only one of the titles for this page. Otherwise, you may delete it. Use this page for your
875 epilogue or conclusion if applicable; please use only one of the titles for this page. Otherwise,
876 you may delete it. Use this page for your epilogue or conclusion if applicable; please use only one
877 of the titles for this page. Otherwise, you may delete it. Use this page for your epilogue or
878 conclusion if applicable; please use only one of the titles for this page. Otherwise, you may delete
879 it. Use this page for your epilogue or conclusion if applicable; please use only one of the titles for
880 this page. Otherwise, you may delete it. Use this page for your epilogue or conclusion if
881 applicable; please use only one of the titles for this page. Otherwise, you may delete it. Use this
882 page for your epilogue or conclusion if applicable; please use only one of the titles for this page.
883 Otherwise, you may delete it. Use this page for your epilogue or conclusion if applicable; please
884 use only one of the titles for this page. Otherwise, you may delete it. Use this page for your
885 epilogue or conclusion if applicable; please use only one of the titles for this page. Otherwise,
886 you may delete it. Use this page for your epilogue or conclusion if applicable; please use only one
887 of the titles for this page. Otherwise, you may delete it. Use this page for your epilogue or
888 conclusion if applicable; please use only one of the titles for this page. Otherwise, you may delete
889 it.

References

- 891 [1] Jens Erler and Paul Langacker. “Electroweak model and constraints on new physics”. In:
 892 (July 2004). arXiv: hep-ph/0407097.
- 893 [2] David J Griffiths. *Introduction to elementary particles; 2nd rev. version*. Physics textbook.
 894 New York, NY: Wiley, 2008.
- 895 [3] M. Tanabashi et al. “Review of Particle Physics”. In: *Phys. Rev. D* 98 (3 2018), pp. 847–851.
- 896 [4] E. Noether. “Invariante Variationsprobleme”. In: *Nachr. d. König. Gesellsch. d. Wiss. zu
 897 Göttingen, Math-phys. Klasse, Seite 235-157* (1918). eprint: www.physics.ucla.edu/
 898 \~\cwp/articles/noether.trans/german/emmy235.html.
- 899 [5] J. H. Christenson et al. “Evidence for the 2π Decay of the K_2^0 Meson”. In: *Phys. Rev. Lett.*
 900 13 (1964), pp. 138–140.
- 901 [6] J. E. Augustin et al. “Discovery of a Narrow Resonance in e^+e^- Annihilation”. In: *Phys.
 902 Rev. Lett.* 33 (1974), pp. 1406–1408.
- 903 [7] J. J. Aubert et al. “Experimental Observation of a Heavy Particle J ”. In: *Phys. Rev. Lett.* 33
 904 (1974), pp. 1404–1406.
- 905 [8] Martin L. Perl et al. “Evidence for Anomalous Lepton Production in e+ - e- Annihilation”.
 906 In: *Phys. Rev. Lett.* 35 (1975), pp. 1489–1492.
- 907 [9] S. W. Herb et al. “Observation of a Dimuon Resonance at 9.5-GeV in 400-GeV Proton-
 908 Nucleus Collisions”. In: *Phys. Rev. Lett.* 39 (1977), pp. 252–255.
- 909 [10] F. Abe et al. “Observation of top quark production in $\bar{p}p$ collisions”. In: *Phys. Rev. Lett.* 74
 910 (1995), pp. 2626–2631. arXiv: hep-ex/9503002.
- 911 [11] S. Abachi et al. “Observation of the top quark”. In: *Phys. Rev. Lett.* 74 (1995), pp. 2632–
 912 2637. arXiv: hep-ex/9503003.
- 913 [12] K. Kodama et al. “Observation of tau neutrino interactions”. In: *Phys. Lett. B* 504 (2001),
 914 pp. 218–224. arXiv: hep-ex/0012035.
- 915 [13] G. Arnison et al. “Experimental Observation of Lepton Pairs of Invariant Mass Around 95-
 916 GeV/c**2 at the CERN SPS Collider”. In: *Phys. Lett. B* 126 (1983), pp. 398–410.

- 917 [14] P. Bagnaia et al. “Evidence for $Z^0 \rightarrow e^+e^-$ at the CERN $\bar{p}p$ Collider”. In: *Phys. Lett. B* 129
 918 (1983), pp. 130–140.
- 919 [15] Serguei Chatrchyan et al. “Observation of a New Boson at a Mass of 125 GeV with the
 920 CMS Experiment at the LHC”. In: *Phys. Lett. B* 716 (2012), pp. 30–61. arXiv: 1207.7235
 921 [hep-ex].
- 922 [16] Georges Aad et al. “Observation of a new particle in the search for the Standard Model
 923 Higgs boson with the ATLAS detector at the LHC”. In: *Phys. Lett. B* 716 (2012), pp. 1–29.
 924 arXiv: 1207.7214 [hep-ex].
- 925 [17] K. G. Begeman, A. H. Broeils, and R. H. Sanders. “Extended rotation curves of spiral galax-
 926 ies: Dark haloes and modified dynamics”. In: *Mon. Not. Roy. Astron. Soc.* 249 (1991), p. 523.
- 927 [18] Y. Ashie et al. “Evidence for an oscillatory signature in atmospheric neutrino oscillation”.
 928 In: *Phys. Rev. Lett.* 93 (2004), p. 101801. arXiv: hep-ex/0404034.
- 929 [19] C. Abel et al. “Measurement of the Permanent Electric Dipole Moment of the Neutron”. In:
 930 *Phys. Rev. Lett.* 124.8 (2020), p. 081803. arXiv: 2001.11966 [hep-ex].
- 931 [20] Guillaume Albouy et al. “Theory, phenomenology, and experimental avenues for dark show-
 932 ers: a Snowmass 2021 report”. In: *The European Physical Journal C* 82.12 (Dec. 2022).
- 933 [21] Lyndon Evans and Philip Bryant. “LHC Machine”. In: *Journal of Instrumentation* 3.08
 934 (2008), S08001.
- 935 [22] “The ATLAS Experiment at the CERN Large Hadron Collider”. In: *JINST* 3 (2008). Also
 936 published by CERN Geneva in 2010, S08003.
- 937 [23] “The CMS experiment at the CERN LHC”. In: *Journal of Instrumentation* 3.08 (2008),
 938 S08004.
- 939 [24] “The ALICE experiment at the CERN LHC”. In: *Journal of Instrumentation* 3.08 (2008),
 940 S08002.
- 941 [25] “The LHCb Detector at the LHC”. In: *Journal of Instrumentation* 3.08 (2008), S08005.
- 942 [26] Ana Lopes and Melissa Loyse Perrey. *FAQ-LHC The guide*. 2022.
- 943 [27] Esma Mobs. “The CERN accelerator complex in 2019. Complexe des accélérateurs du
 944 CERN en 2019”. In: (2019). General Photo.
- 945 [28] *Pulling together: Super Conducting electromagnets*. <https://home.cern/science/engineering/pulling-together-superconducting-electromagnets>.
 946 Accessed: 2024-01-05.

- 948 [29] *The High-Luminosity LHC*. <https://voisins.web.cern.ch/en/high-luminosity-lhc-hl-lhc>. Accessed: 2024-01-05.
- 950 [30] Aad G., et al. (ATLAS Collaboration and CMS Collaboration). “Combined Measurement of
951 the Higgs Boson Mass in pp Collisions at $\sqrt{s} = 7$ and 8 TeV with the ATLAS and CMS
952 Experiments”. In: *Phys. Rev. Lett.* 114 (19 2015), p. 191803.
- 953 [31] O. Aberle et al. *High-Luminosity Large Hadron Collider (HL-LHC): Technical design re-*
954 *port*. CERN Yellow Reports: Monographs. Geneva: CERN, 2020.
- 955 [32] The ATLAS Collaboration. “The ATLAS Experiment at the CERN Large Hadron Collider”.
956 In: *Journal of Instrumentation* 3.08 (2008), S08003.
- 957 [33] G Aad, B Abbott, and ATLAS Collaboration. “Performance of the reconstruction of large
958 impact parameter tracks in the inner detector of ATLAS”. In: *Eur. Phys. J. C Part. Fields*
959 83.11 (Nov. 2023).
- 960 [34] Joao Pequenao. *Computer Generated image of the ATLAS calorimeter*. 2008.
- 961 [35] *ATLAS liquid-argon calorimeter: Technical Design Report*. Technical design report. AT-
962 LAS. Geneva: CERN, 1996.
- 963 [36] H A Gordon. “Liquid argon calorimetry for the SSC”. In: () .
- 964 [37] Henric Wilkens and (on behalf of the ATLAS LArg Collaboration). “The ATLAS Liquid
965 Argon calorimeter: An overview”. In: *Journal of Physics: Conference Series* 160.1 (2009),
966 p. 012043.
- 967 [38] *Technical Design Report for the Phase-II Upgrade of the ATLAS Tile Calorimeter*. Tech.
968 rep. Geneva: CERN, 2017.
- 969 [39] “Technical Design Report for the Phase-II Upgrade of the ATLAS Muon Spectrometer”. In:
970 () .
- 971 [40] L Pontecorvo. “The ATLAS Muon Spectrometer”. In: (2004). revised version number 1
972 submitted on 2003-07-27 16:31:16.
- 973 [41] *ATLAS magnet system: Technical Design Report, 1*. Technical design report. ATLAS. Geneva:
974 CERN, 1997.
- 975 [42] Joao Pequenao. “Event Cross Section in a computer generated image of the ATLAS detec-
976 tor.” 2008.
- 977 [43] ATLAS Collaboration. “ATLAS Experiment Implements Heterogeneous Particle Recon-
978 struction with Intel oneAPI Tools”. General Photo. 2023.

Appendix A: Experimental Equipment

981 Lorem ipsum dolor sit amet, consectetur adipiscing elit, sed do eiusmod tempor incididunt ut
982 labore et dolore magna aliqua. Ut enim ad minim veniam, quis nostrud exercitation ullamco laboris
983 nisi ut aliquip ex ea commodo consequat. Duis aute irure dolor in reprehenderit in voluptate velit
984 esse cillum dolore eu fugiat nulla pariatur. Excepteur sint occaecat cupidatat non proident, sunt in
985 culpa qui officia deserunt mollit anim id est laborum.

986

987

Appendix B: Data Processing

988 Lorem ipsum dolor sit amet, consectetur adipiscing elit, sed do eiusmod tempor incididunt ut
989 labore et dolore magna aliqua. Ut enim ad minim veniam, quis nostrud exercitation ullamco laboris
990 nisi ut aliquip ex ea commodo consequat. Duis aute irure dolor in reprehenderit in voluptate velit
991 esse cillum dolore eu fugiat nulla pariatur. Excepteur sint occaecat cupidatat non proident, sunt in
992 culpa qui officia deserunt mollit anim id est laborum.